TECHNISCHE UNIVERSITÄT WIEN

Diplomarbeit

Development of Monte Carlo simulations for characterization and optimization of TOCCSL experiments

ausgeführt am

Institut für Angewandte Physik

der Technischen Universität Wien

unter Anleitung von

Univ.Prof. Dipl.-Ing. Dr.techn. Gerhard Schütz

und

Univ.Ass. Dipl.-Ing. Dr.techn. Mario Brameshuber

durch

Dominik Kiesenhofer

Oberer Markt 3

3361 Aschbach-Markt

Wien, am 20.10.2017

Danksagung

Eine Seite dieser Arbeit soll genutzt sein, um einigen Personen meinen Dank auszusprechen. In diesem Sinne danke ich zuerst allen MitarbeiterInnen und DiplomandInnen der Biophysik-Gruppe der TU Wien, die ein sehr lehrreiches und gleichzeitig auch äußerst entspanntes und lustiges Umfeld während meiner Diplomarbeit waren. Besonderer Dank gilt Gerhard Schütz und Mario Brameshuber für die vielen positiven Eindrücke, die ich aufgrund ihrer Begeisterung für die Wissenschaft und im Speziellen für die Biophysik erfahren durfte und für alles, was ich dabei lernen konnte. Außerordentlich dankbar bin ich Mario, der trotz seines vollen Kalenders immer Zeit für Gespräche gefunden hat und zuletzt sogar das ein oder andere Wochenende für das Lesen dieser Diplomarbeit geopfert hat. Seine herzliche, geduldige und konstruktive Betreuung hat mir die Arbeit im letzten Jahr sehr angenehm gemacht. Ich möchte auch Andreas Arnold danken - vor allem für die Reduktion der Aktivierungsenergie zu Beginn meiner Arbeit durch zahlreiche hilfreiche Tipps.

Von ganzem Herzen bedanken möchte ich mich bei meiner Familie, allen voran meinen Eltern, die mich immer bedingungslos unterstützt haben. Ich weiß das sehr zu schätzen.

Danke an meine Studienfreunde, für ihre Gesellschaft und offenen Ohren in den Mittags- und Kaffeepausen, aber auch weit abseits davon.

Danke an alle anderen WeggefährtInnen der letzten Jahre und an all jene, die hier nicht erwähnt sind, jedoch erwähnenswert gewesen wären.

Danke!

Contents

1 Abstract

A previously developed single-molecule microscopy technique termed TOCCSL (thinning out clusters while conserving stoichiometry of labeling) allows for direct imaging and stoichiometric analysis of molecular aggregates diffusing in the plasma membrane at high surface densities. The method is based on photobleaching of a confined area and subsequent imaging at the onset of the recovery process. Brightness analysis of individual diffraction-limited spots reveals the distribution of oligomeric fractions. In the present work, Monte Carlo-based computer simulations of TOCCSL experiments were developed to study the influence of three major sources of error on the experimental outcome: incomplete photobleaching of aggregates, oligomerization state-dependent mobility differences and false-positive oligomer detection due to random encounters. Trajectories of randomly diffusing particles are implemented as a Gaussian random walk. The photobleaching probability for individual particles is stochastically determined according to measured photobleaching curves of GPI-anchored monomeric GFP in the plasma membrane of CHO cells. TOCCSL simulations with varying parameters were performed to characterize individual and combined error sources. With regard to these simulations, strategies are discussed in order to optimize the accuracy of measurements by adjustment of experimental parameters and data post-processing.

2 Introduction

2.1 General introduction

Over recent decades, single molecule microscopy and especially the establishment of total internal reflection fluorescence microscopy have resulted in uncountable revolutionary findings and developments. Single molecule microscopy is an outstanding tool for unraveling protein lateral organization and dynamics in cells. As there are many well-established techniques for the detection of protein-protein interaction, most of them are based on bulk experiments or performed in solution. At the time being, however, there is no straightforward implementation of tools to quantify the stoichiometric composition of protein (or lipid) complexes in the plasma membrane - a question, which is of central interest in cell biology.

A major limitation for the measurement of protein-protein interactions in the membrane of live cells is the typically high surface density of target proteins. Therefore, a single molecule

technique termed TOCCSL (Thinning Out Clusters while Conserving the Stoichiometry of Labeling) was recently established, which allows for direct visualization of protein aggregation and dynamics in the plasma membrane of live cells at arbitrarily high expression levels. The method is based on a simple photobleaching and imaging protocol and, thus, relatively easy to implement. Despite the approach's simplicity, there are some influences on the experimental outcome, that should be taken into account when employing this technique. The most important impacts are incomplete photobleaching of aggregates, oligomerization state-dependent mobility differences and false-positive oligomer detection due to random encounters. Since the TOCCSL technique is very promising as an easy-to-use technique for the investigation of aggregation in the plasma membrane, it is essential to provide a reliable foundation by careful consideration of these effects on the results. The desire for deeper understanding and quantification of influencing factors on a TOCCSL experiment constitutes the motivation of this work. As the establishment of analytical solutions for these problems is not feasible, a stochastic computer simulation based on simple Monte Carlo techniques constitutes the method of choice. The development of simulation algorithms and the investigation of the impact of various parameters on the experiments are discussed in the framework of this diploma thesis.

2.2 The cell membrane

The cell (or plasma) membrane separates the cytosolic interior of the cell from its extracellular environment and is therefore crucial to the life of the cell. It consists of a lipid double layer (bilayer) of about 5 nm thickness. The hydrophilic headgroups of the lipids are facing outwards, whereas the hydrophobic chains constitute the interior of the membrane. The lipid bilayer, held together by non-covalent interactions, is almost impermeable to most water-soluble molecules due to its hydrophobic internal structure. It contains a large number of proteins and it is estimated that about 30 % of the proteins encoded in an animal cell's genome are membrane proteins [1]. The fluidity of a lipid bilayer depends strongly on its lipid composition, which is widely studied by investigation of synthetic bilayers. The three most important lipids in cell membranes are phosphoglycerides, sphingolipids and sterols, such as cholesterol. The membrane is selectively permeable to ions and molecules. Specialized proteins called *ion channels*, provide for ion gradients and, consequently, the generation of an electrochemical potential. This mechanism can be used to store energy by synthesizing adenosin triphosphate (ATP), drive

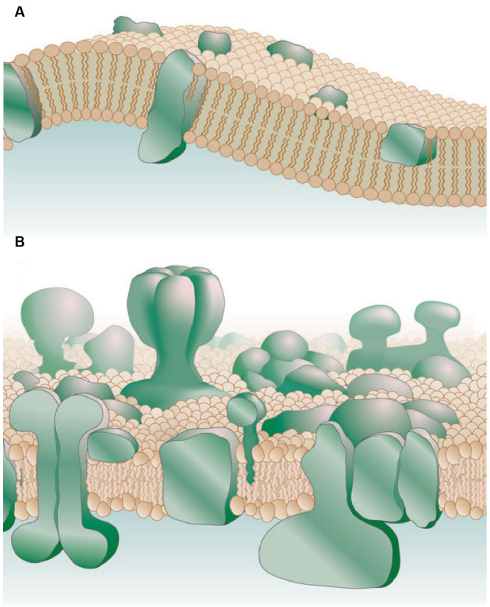

Figure 1: Illustration of the plasma membrane. (**A**) *Fluid mosaic membrane model* by *Singer and Nicolson*. (**B**) Updated model of a crowded plasma membrane with variable patchiness and thickness according to [3]. Figure adapted from [3].

the transmembrane movement of selected solutes or produce and transmit electrical signals as it is the case for nerve and muscle cells. Certain protein sensors, so-called *receptors*, cause ligand-induced responses to environmental cues and transfer information across the membrane. A receptor protein only binds with ligands of a specific chemical structure, leading to activation or inhibition of the receptor's associated signaling pathway.

Probably the most prominent and influential model of the plasma membrane has been posed by Singer and Nicolson in 1972 [2]. According to their *fluid mosaic model*, the cell membrane is considered a two-dimensional fluid. Individual lipid molecules and membrane proteins are more or less free to diffuse laterally within the unperturbed bilayer. The model includes that the proteins are dispersed, mainly monomeric and at low concentration (Fig. 1A). The scientific developments in recent decades, however, have weakened the generalizations of this model and raised the need for a new paradigm. The discussion about *lipid rafts* is a good example for the ongoing development of scientific findings regarding the plasma membrane [4]. Nowadays, it is known that the plasma membrane is usually densely populated and not as random and not as homogeneous as it was assumed to be in former models [3]. Membrane proteins can be organized in large functional complexes and lipids as well as proteins tend to group together, forming lipid-lipid and lipid-protein interactions. The thickness of the bilayer varies considerably due to

distortions of the lipids in order to cover the hydrophobic area of membrane proteins. It results in curvature of the membrane and can influence protein interactions. Besides free diffusion of particles, as it is shown by single-particle tracking experiments [5], there is a complex set of restrictions on protein lateral mobility such as crowding, ectodomain collisions, transbilayer interactions, adhesion sites and cytoskeletal structure [6]. Different mechanisms lead to anomalous diffusion, confined or directed motion, which seem to be ubiquitous, although many proteins are found to diffuse relatively freely. Thus, the plasma membrane seems to be much more versatile than originally expected, making it an interesting field for ongoing discoveries.

2.3 Oligomerization of proteins

Many processes, such as signaling processes, inside the cell and at the cell surface depend on protein-protein interaction and oligomerization of proteins. Some signaling processes, for instance, only occur after (ligand-induced) oligomerization of certain proteins. The same non-covalent bonds and forces enabling a protein to fold into a certain conformation can lead to the interaction of two or more separate subunits, overcoming the entropy that favors monomeric proteins. These include hydrogen bonds, ion pairs, the interaction of helix dipoles, packing differentials involving lipid/protein interactions, interactions with prosthetic groups and external constraints such as links between helices of membrane proteins or interactions with other molecules [7, 8]. Associations occur between the same type of proteins (homo-association) or different kinds of proteins (hetero-association). Receptor proteins in the cell membrane have a key role in transmitting a signal across the plasma membrane upon a certain stimulus. Many of these receptors start to interact with other molecules (e.g. other receptors) after a stimulus has occurred and form larger aggregates. Therefore the investigation of oligomerization and stoichiometry of proteins is crucial for understanding and unravelling the functionality of proteins and their role in associated processes. As an example, the presence of epidermal growth factor (EGF) in the extracellular region leads to conformational changes of the EGF receptor upon binding the EGF. This triggers the ligand-induced dimerization of the EGF receptor, followed by trans-auto-phosphorylation - a crucial step for transmission of a signal across the membrane within the EGFR signaling pathway [9]. This demonstrates that the oligomerization of proteins is essential for particular processes in the plasma membrane. Numerous membrane proteins can be found in different oligomeric states. In some cases, an active site for ligand binding

is introduced at the interface between subunits [10], initializing the interaction between the oligomerized aggregate and other molecules.

2.4 Techniques for determination of stoichiometry

The importance of and the interest in the investigation of protein-protein interaction and aggregation has lead to different approaches for studying the stoichiometry of proteins. Several of them can routinely be performed in solution. A simple and powerful method for detecting and characterizing protein oligomerization is based on affinity purification via co-immunoprecipitation (co-IP) . It is well-suited for hetero-oligomerization, but has its limits in order to detect homo-association because the molecule of interest has to be modified by attaching two different tags for co-IP. Major drawbacks are the loss of spatial organization during cell lysis and that weakly interacting complexes do not endure the purification process, if not stabilized by photocrosslinking [11]. Another method utilizes biotinylation of proteins within the same clusters by fusing a horseradish peroxidase to a target protein. An active radical species of arylazide biotin is produced on the protein finally binding to other biotinylated proteins. Subsequent content analysis is done via Western blotting [12].

As membrane proteins have proven to be difficult to analyze by various complementation assays [13], other techniques have to be taken into account. Förster resonance energy transfer (FRET) between a donor and an acceptor dye is a common bulk technique to quantify oligomerization at the live cell plasma membrane, however, the interpretation of results is complicated by the lack of precise knowledge of the respective concentrations and spectral properties of the dyes involved. Correlation methods such as number and brightness analysis [14, 15], or cross-correlation analysis [16, 17] are also frequently used to obtain information on oligomerization.

All these methods are based on bulk experiments, whereby only average values can be determined. Thus, the analysis and interpretation of data are often difficult. In order to quantify and observe the dynamics and states of molecular association, it is necessary to make use of single molecule imaging methods [18]. Even association and dissociation of two differently labeled membrane proteins can directly be captured in real-time, like it was achieved in [19] for the dimerization of the receptor tyrosine kinase ErbB1 by two-color single particle tracking using photo-stable quantum dots. A recent study used a two-color coincidence analysis for detecting G-protein coupled receptor oligomerization and compared results with well-characterized control

proteins [20]. The direct observation of dimerization could be extended to the determination of stoichiometry of higher order oligomers by counting individual bleaching steps of fluorescent markers on immobilized protein complexes upon continuous illumination [21, 22].

The single molecule techniques described above, have in common that very low surface densities of the fluorescently labelled target protein (below one molecule per μm^2) are required to unambiguously resolve individual molecules or aggregates. Typical surface densities of endogenous proteins, however, can be expected to be orders of magnitude higher. In this regard, super-resolution techniques like PALM [23], fPALM [24], STORM [25] or dSTORM [26] come into consideration as single molecule approaches at high expression levels. These techniques, in principle, allow for quantitative stoichiometry analysis [27, 28]. They are able to resolve structures below the diffraction limit of light but are generally restricted to fixed cells, unless probe movement during the recording time of the super-resolution images is small compared to the desired resolution [18]. The procedure, however, is prone to artifacts [29–32], possibly affecting the protein oligomeric state. The main issues concerning these super-resolution techniques are unknown blinking-characteristics of fluorescent probes and the diffraction-limited resolution. Due to these limitations, the stoichiometry analysis of small clusters at physiological expression levels is, particularly in live cells, out of reach.

In order to resolve the issues of high surface densities in live cell experiments and artifacts in fixed cells the TOCCSL technique was established. In [33], proof of concept has been demonstrated on a model system with surface densities, which do not allow for straightforward imaging. Since then, it has been applied and further developed in several works [34–39]. The TOCCSL technique is described in detail in Sec. 2.5.

PhotoGate microscopy [40] is another recently developed single molecule technique, which is similar to the TOCCSL assay. There, the boundary of the region of interest (ROI) is repeatedly photobleached in order to keep the surface density within the ROI at a constant low level. This enables the recording of long trajectories of individual molecules or aggregates within the imaged region. The repetitive photobleaching of the boundary is realized by a piezo-driven mirror, that sweeps a high intensity laser beam repeatedly around the ROI. Utilizing this method the dynamics of signaling molecules on early endosomes and the ligand-induced dimerization of EGF receptors could be observed and quantified at high surface densities in live cell experiments. Stoichiometry analysis was done by analysis of photobleaching steps of the fluorescent dyes.

2.5 The TOCCSL technique

Thinning out clusters while conserving the stoichiometry of labeling is a method used for the stoichiometric analysis of molecular aggregates in biomembranes. It is based on single molecule fluorescence microscopy. Basically, it constitutes an extension of the well-established fluorescence recovery after photobleaching (FRAP) technique to the single-molecule level. In live cells, a highly expressed membrane protein typically leads to surface densities of hundreds of molecules per μm^2. Given such high densities, it is impossible to resolve individual signals of single aggregates due to the diffraction limit. By applying a simple photobleaching and imaging protocol, brightness analysis of individual aggregates and subsequent determination of the stoichiometry is enabled. After recording a pre-bleach image at a low illumination intensity (Fig. 2a), a small region (typically around $10-100$ μm^2) of the cell membrane is exposed to a high intensity laser pulse for a well-defined time t_{bleach} (Fig. 2b). An adjustable slit aperture is usually used as a field stop to restrict the photobleached area. The photobleaching pulse ideally results in complete photobleaching of fluorescence within the illuminated region, which a control image enables to check for. Due to Brownian motion, fluorescent molecules enter the bleached region from the shielded part of the membrane. Images are recorded at the very onset of this recovery process after the recovery time t_{rec} (Fig. 2d). The recovery time is chosen such that a low surface density in the inner region allows for resolving individual diffraction limited spots of single molecules or aggregates. The proper choice of t_{rec} depends on the size of the photobleached region (controlled by aperture size), the surface density of fluorescent probes and the diffusion coefficient D of the observed molecule. The statistical distribution of fluorescent probes per aggregate is determined via brightness analysis of individual signals.

A TOCCSL experiment is based on measuring the fluorescence intensity of individual diffraction-limited spots. Due to the stochastic emission process, the number of detected photons F from a single spot is characterized by a probability density function (pdf). Given a mixed population of monomers and various types of oligomers, the resulting pdf for the fluorescence intensity of measured spots $\rho(F)$ is represented by a linear combination of the intensity pdfs for the respective N-mer population $\rho_N(F)$ with N colocalized independent emitters (Fig. 3B)

$$\rho(F) = \sum_{N=1}^{N_{max}} \alpha_N \cdot \rho_N(F). \tag{1}$$

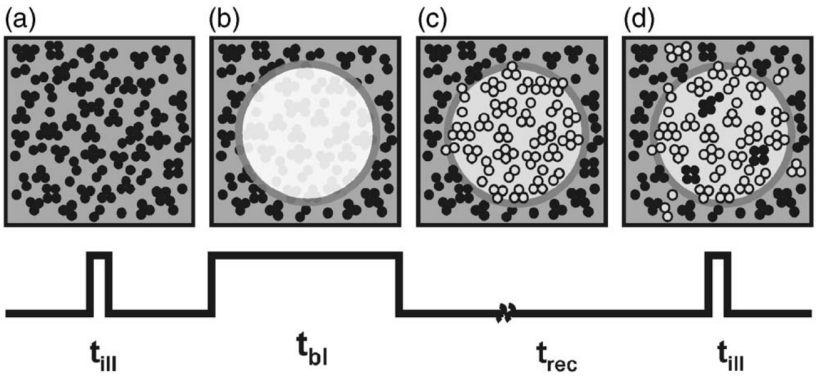

Figure 2: Schematic model of the TOCCSL method. The top row represents images of the sample, the bottom row the respective timing protocol for illumination. **(a)** A pre-bleach image is recorded (with illumination time t_{ill}) showing the initial situation at typically high surface densities. **(b)** Fluorescent molecules within a well-defined region are photobleached by an extended high intensity laser pulse during t_{bl}. The molecules outside the illuminated region remain unaffected. **(c)** Immediately after photobleaching, the illuminated area contains only non-fluorescent biomolecules (open circles). **(d)** During the recovery time t_{rec} fluorescent aggregates diffuse into the bleached region. The TOCCSL image containing individual diffraction limited spots is recorded for brightness analysis after t_{rec}.

$\rho(F)dF$ denotes the probability that the number of detected photons from a single diffraction-limited spot is given within the interval $[F, F+dF]$. The weights of the individual distributions, α_N, with $\sum_{N=1}^{N_{max}} \alpha_N = 1$ correspond to the relative fractions of the respective oligomer of degree N. The values of α_N can be determined by fitting the measured curve for ρ_N with Eq. 1.

Beforehand, the ρ_N have to be calculated from the single-dye intensity pdf ρ_1 (Fig. 3A). The corresponding intensity distribution of N colocalized independent emitters, $\rho_N(F)$, can be determined recursively as a series of convolution integrals

$$\rho_N(F) = \int \rho_1(F')\rho_{N-1}(F-F')dF'. \tag{2}$$

The fluorescence intensity values of individual fluorophores for $\rho_1(F)$ can be acquired in separate experiments or by additional photobleaching of a sample. Photobleaching leads to a stepwise fluorescence decrease, assuming higher order oligomers present before. After extensive photobleaching, only a few fluorescent spots are still visible in the illuminated area. The probability to detect more than one active fluorescent dye per spot is negligible. The stepwise photobleaching process can also be observed and analyzed in order to ensure that the lowest intensity level within one photobleaching trace is used to determine ρ_1.

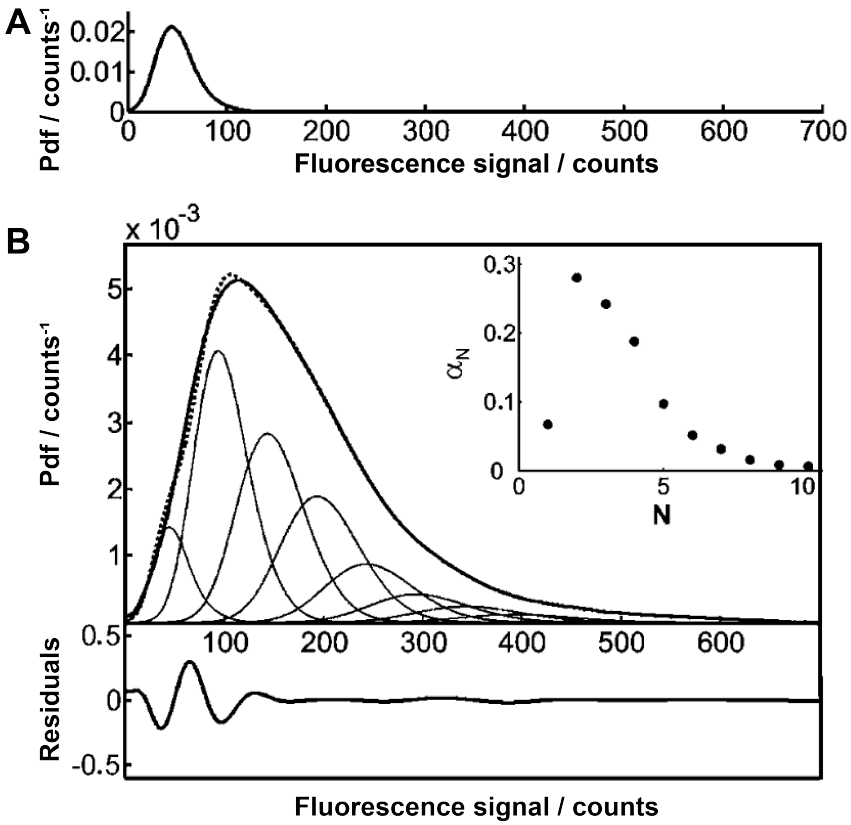

Figure 3: Quantification of the cluster load of fluorescein-labeled antibodies via TOCCSL. **A** The probability density function for the fluorescence intensity of a single fluorophore ρ_1 is shown. ρ_1 can be used for calculation of ρ_N for multiple emitters. **B** The solid line shows the measured probability density function, which was fitted (dotted line) using Eq. 1. The weighted contributions of the individual N-mers $\alpha_N \cdot \rho_N$ are plotted as thin lines. The inset shows the distribution of cluster load N, where the dominant species, in this case, was found to be dimers with a long tail towards high N. The residuals do not indicate any significant deviation over the full fitting range. Image adapted from [33].

2.5.1 A typical TOCCSL setup

A typical TOCCSL setup as shown in Fig. 4 is based on a total internal reflection fluorescence (TIRF) microscope. A key component of the setup is the field stop (typically a slit aperture) in order to confine the photobleached region. The main components of a typical TOCCSL setup are briefly described in the following.

1. Coherent light source / Laser

   Different lasers of distinct wavelengths allow for excitation and photoswitching of a variety of fluorophores. Typically three different lasers with wavelengths of 488 nm, 532 nm and 647 nm are implemented to cover a certain excitation spectrum. For photoswitchable fluorophores, most commonly a 405 nm and a 561 nm laser are used for switching and imaging,

respectively. Directly modulated lasers or lasers equipped with mechanical shutters and accousto-optical modulators allow for a fast and precise adjusting of illumination timing.

2. High-speed piezo table with mirror

   A mirror mounted on a high-speed piezo table is used to impose a parallel shift on the laser beams, which allows for fast switching between Non-TIR, light sheet (HILO) [41] or TIR illumination with switching times below 30 ms. For cellular systems featuring a high background of cytosolic fluorescence, bleaching in non-TIR configuration and switching to TIR for the TOCCSL image typically yields an improved signal-to-noise ratio.

3. Aperture

   In a simple case an adjustable slit aperture positioned in a sample-conjugated plane can be used to confine the laser to a well-defined region for both bleaching and read-out. The position of the aperture is critical for formation of a sharp image but restricted by the geometry of the imaging system. Photobleaching of arbitrary shapes could be implemented by an xy-laser scanning unit. Switching between different illumination configurations is then achieved by combination with a fast-switching mirror.

4. EMCCD camera

   Signals are detected via an electron-multiplying CCD camera. Low noise at high read-out speed yields a high sensitivity and even allows for detection of single photons due to electron multiplying.

5. Image splitter

   In a 2-color-TOCCSL experiment, an image splitter is used to separate the emission from two spectrally distinct fluorophores into two detection channels on the same camera chip.

2.5.2 TOCCSL modalities

TOCCSL as a single molecule microscopy technique is suitable for combination with other fluorescence microscopy tools such as multicolor detection for colocalization studies (see next section) or FRET analysis for assaying cluster size and substructures. The TOCCSL approach, in general, holds the possibility of studying nano-structures under physiological conditions. The functional consequence of a trigger, such as changes in environmental conditions or the application of external ligands, can be observed as a structural modification in the plasma membrane.

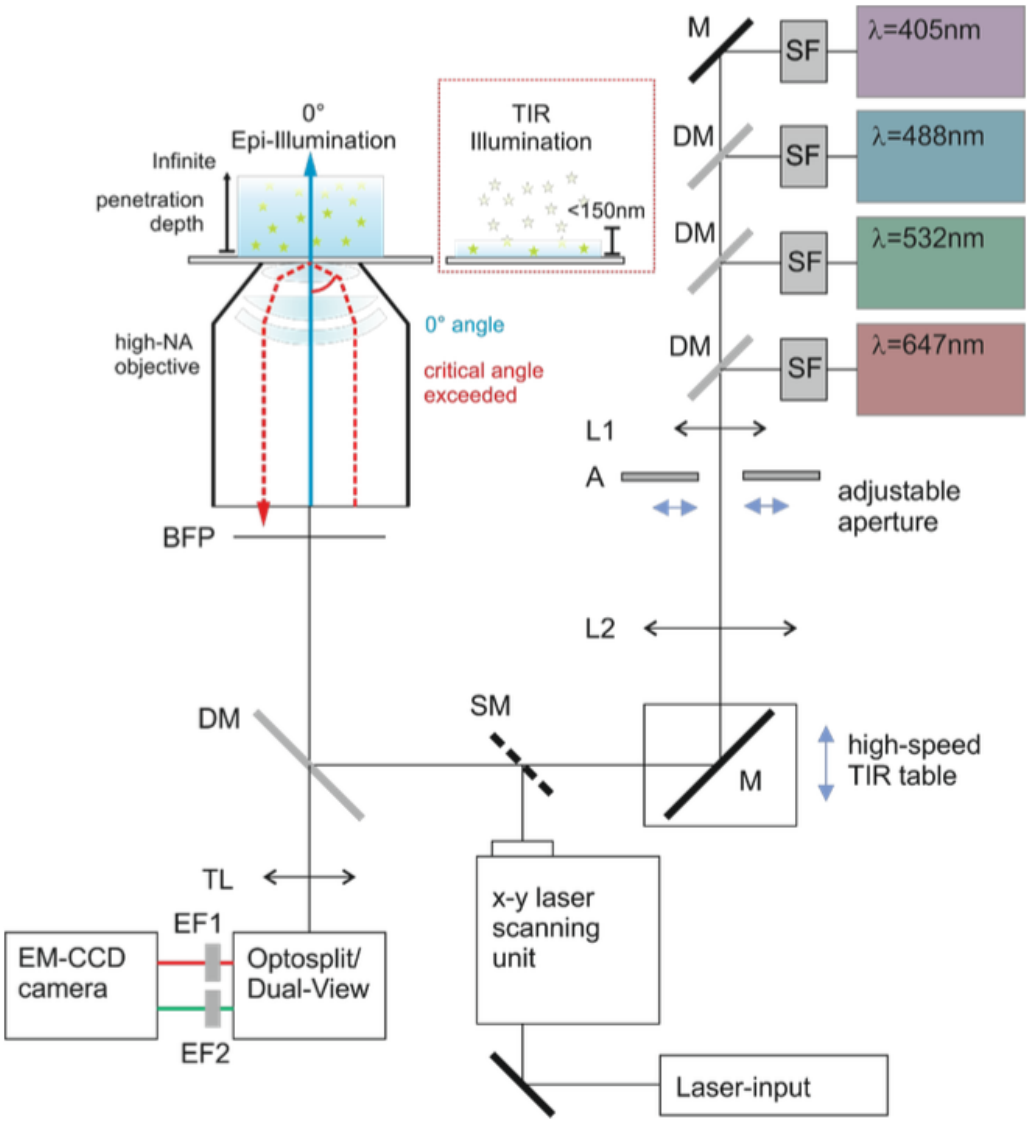

Figure 4: Schematic drawing of a possible TOCCSL setup. Laser beams from different sources are spatially filtered (SF) and overlaid with dichroic mirrors (DM). The combined laser beams pass an adjustable aperture (A) positioned in a sample-conjugated plane, and are focused by a lens system (L1 and L2) onto the back focal plane (BFP) of a high-NA oil immersion objective. By moving a mirror (M) mounted on a high-speed piezo table, the laser beams can be shifted parallel with regard to the optical axis. This allows for fast switching between non-TIR, HILO or TIR illumination. The fluorescence signal is collected by the same objective, separated from excitation light by a dichroic mirror (DM), and imaged via the tube lens (TL) onto an EM-CCD camera. For splitting emission into two detection channels, the Optosplit or Dual-View system, equipped with an appropriate dichroic mirror and two emission filters (EF1/2), can be used. A supplementary xy-laser scanning unit with a switchable mirror (SM) allows for bleaching arbitrary shapes in the sample plane. Figure courtesy of Mario Brameshuber.

Up to now, TOCCSL has exclusively been used for the investigation of mobile molecules, which are entering the photobleached area during a specified recovery time. Typically, however, a significant fraction of molecules does not contribute to the analyzed mobile population. The implementation of an inverse TOCCSL approach could, in principle, allow for probing immobile molecules. This could be realized by photobleaching concentric rings around a central circular region of interest, e.g. with a piezo-driven mirror. In the central ROI, mainly immobile molecules would remain, whereas mobile particles dissipate into the bleached region. By doing so, the characterization of immobile molecules in terms of oligomerization, spatial organization by super-resolution microscopy and kinetics of immobilization are within reach.

2.5.3 Two-color TOCCSL

As mentioned before, TOCCSL experiments can be extended to two-color microscopy. Thus, extremely rare molecular interactions (down to 2.5 % interaction probability) can be observed and identified unambiguously [35]. This is important since cell biological processes, particularly signaling processes, are often initiated by these rare interactions. Two-color TOCCSL is suitable for biomembranes containing molecules of species A and B, which are labeled with a red and a green fluorophore, respectively. The surface densities of both species are typically too high for resolving single molecules as individual diffraction-limited spots. As in a single-color TOCCSL experiment, a small region of the sample cell membrane is photobleached with high laser power. A TOCCSL image is recorded at the onset of the subsequent fluorescent recovery process. The signals of two spectrally distinct fluorophores are separated into two color channels by an image splitter and imaged to different locations on the same camera chip. If a signal is localized within a certain radius in both channels, it is regarded as a colocalization of molecules A and B. Further information such as the brightness in each spectral channel, the distance between the green and red label or FRET-based analysis may be used for a more detailed characterization of the clusters. The accuracy of measurements can even be improved and complemented by single molecule tracking data of two bound molecules as an additional criterion to rule out the possibility of accidental colocalizations.

2.6 Monte Carlo simulations of TOCCSL experiments

In theory, the TOCCSL technique is based on a relatively simple approach in order to determine the oligomerization states of proteins. However, conducting a TOCCSL experiment (especially in live cells) exceeds the simplicity of an idealized model assuming instantaneous photobleaching, well-known diffusive behavior etc. and can lead to variations of the experimental outcome. The results could be influenced by error sources like incomplete bleaching of aggregates with multiple fluorophores due to a finite bleaching time, false colocalizations or mobility differences for different molecular species. In addition, various experimental parameters like bleaching time, recovery time or aperture size are more or less variable. The proper choice of these parameters depends, amongst others, on the surface density and the diffusive properties of the target protein. They are, however, still variable to a certain degree without knowing the effects on the results. This raises a number of questions like: *How is the choice of parameters influencing the results? Is there an optimal parameter set? Are there strategies to optimize the accuracy of measurements?*

Due to the complexity of the problem and the multidimensionality of the parameter space, it would be very laborious, if not impossible, to find analytical solutions to answer the posed questions. That is why *in silico* TOCCSL experiments are developed and performed in the framework of this thesis. It is difficult to give a proper definition of the term *Monte Carlo Simulation* since there seems to exist no consensus on the terminology. The distinction between Monte Carlo Simulation, Monte Carlo method, Monte Carlo algorithm, etc. is sometimes not clear. Irrespective of the terminology, Monte Carlo techniques are based on the repeated execution of similar stochastic experiments.In this thesis, the simulations are termed Monte Carlo simulations in the sense that the algorithm uses repeated random sampling. The simulations are based on repeated runs of single stochastic TOCCSL experiments. It could also be referred to as *stochastic simulation*. The random motion of diffusing particles as well as the bleaching process are simulated using simple Monte Carlo methods providing the stochastic nature of underlying physics. A statistical analysis is done for the results of numerous repeated simulation runs. The results should yield deeper insights into TOCCSL experiments and a foundation for optimization of measurements. Furthermore, simulations could, in principle, allow for compensating certain errors by data post-processing.

3 Background

3.1 Fluorescence microscopy

Compared to conventional light microscopy, where contrast is gathered by light absorption, reflection, phase gradients, optical path differences or similar, fluorescence microscopy allows for detection of photons emitted by fluorescent (or phosphorescent) molecules after excitation. Especially in cell biology, fluorescence microscopy has been proven beneficial since it is possible to investigate the distribution, movement and interaction of fluorescently labeled molecules in a specimen, particularly in live cells. For imaging, a fluorophore, typically attached to a non-fluorescent molecule, is illuminated and therefore excited by an appropriate light source, usually lasers but also high-intensity LEDs or nearly monochromatic lamps. The emitted photons can be observed and detected by a camera after passing an emission filter to select the desired wavelength. Dependent on the application and technical implementation, wide field images as well as images of individual fluorescent molecules as diffraction-limited spots can be obtained.

3.1.1 Fluorescence

The phenomenon of fluorescence lays the foundation for fluorescence microscopy and many other applications. Fluorescence, in general, is the emission of photons by a substance that has been excited to a higher electronic state by absorbing electromagnetic radiation. The excitation of electronic states and fluorescence in its entirety can only be described by quantum mechanics and therefore underlies its principles. For excitation of a fluorophore, the presence of photons of a particular excitation wavelength is required. By absorption of a photon of the matching wavelength, the fluorescent molecule is excited to a higher electronic state and relaxes into the ground state shortly after the excitation ($10^{-9} - 10^{-12}$ seconds). The relaxation energy is released again as a photon. Due to energy losses during this process, the wavelength of the emitted photon is typically longer than the wavelength of the absorbed photon (Stokes shift). These energy losses are a result of non-radiative transitions between vibrational or rotational states.

In the majority of cases, the fluorophore is excited from a singlet ground state to a higher singlet state. Alongside the emission of a photon, the relaxation energy can also be released as heat, which is called internal conversion. Furthermore, there is a small probability for the

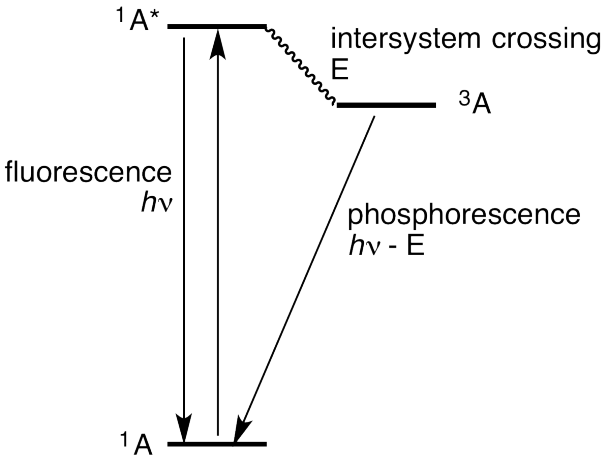

Figure 5: Simplified Jablonski diagram for the energy states of a fluorescent molecule. Fluorescence occurs as an excitation and relaxation process between the two singlet states ^{1}A and ^{1}A* releasing a photon of the energy $E_{ph} = h\nu$. The electronic transition into the triplet state ^{3}A (intersystem crossing) can lead to a quasi-stable configuration and subsequent phosphorescent emission of a photon. Figure adapted under free license from en.wikipedia.org/wiki/Phosphorescence.

electron of relaxing from an excited singlet state to a triplet state, which is called "intersystem crossing" (Fig. 5). This state can be quite stable because the transition into the ground state occurs at a significantly lower rate than for singlet states, resulting in long-lasting storage of the energy of typically milliseconds up to minutes and hours. This phenomenon is referred to as "phosphorescence".

As indicated before, the excitation and emission spectra - exhibiting certain emission and excitation maxima - can be quite distinct, but usually overlap. The detailed spectra of fluorescent molecules are determined by their atomic and electronic structure. Additionally the shapes of spectral curves vary according to the chemical environment affected by pH, ionic composition, polarity, O_2-concentration and others. This has to be taken into account considering the performance of a particular fluorescent molecule.

3.1.2 Fluorescent labeling

Fluorescent labeling is the attachment of a fluorescent molecule to a biomolecule. The multitude of fluorophores, which are commercially available, offers a wide variety of properties like photostability, brightness, quantum yield, fluorescence spectra, etc. As TOCCSL is based on single molecule fluorescence microscopy, fluorescent labeling is of great importance. It is particularly important for TOCCSL experiments that the fluorophores do not tend to oligomerize in order

not to falsify the results. There are several ways to label a target protein (or lipid) with a fluorescent probe, of which the most common labeling techniques are briefly discussed in this section.

Fluorescent proteins

A common method of fluorescent labeling is the genetically encoded fusion of a fluorescent protein to the protein of interest. The gene of the fluorescent protein is artificially fused to the N- or C-terminus of the target protein and introduced into the cell via transfection. The fusion protein is then expressed by the cell itself and by this means the target protein can directly be localized by the fluorescent part of the molecule. It is crucial for experiments that the fusion of the fluorophore does not impair the functionality of the target protein. This labeling method is applicable for membrane proteins as well as intracellular proteins. Probably the most prominent example is the *green fluorescent protein* (GFP). It was originally isolated from the jellyfish *Aequorea victoria* in the 1960s. Currently, there exists a large number of derivates from GFP or other fluorescent proteins. The various mutations have distinct properties regarding excitation and emission wavelength, brightness, photostability and more.

Organic dyes

The fluorescence of organic fluorophores is based on the band transition of delocalized electrons. Compared to fluorescent proteins, organic dyes are generally superior in terms of brightness and photostability. In order to label a particular protein, a ligand is required to attach the fluorophore to the protein.

Immunolabeling

Specific antibodies can be used to label the antigen, that represents the protein of interest. The antibody is fused to a fluorescent molecule (*tag*). Since it is not feasible to fuse a tag to every specific antibody that is requested, usually, a so-called *secondary* antibody is labeled with a fluorophore. The secondary antibody then binds to the *primary* specific antibody. This method is termed *indirect* labeling compared to *direct* labeling of the primary antibody. Unless the target cells are permeabilized, only molecules in the outer leaflet of the plasma membrane can be addressed.

Quantum dots

Quantum dots are fluorescent semiconductor nanoparticles. Since the optoelectronic properties of quantum dots can easily be tuned, e.g by variation of size and shape, they are promising candidates for fluorescent labeling in live cells. So far, there are still some major drawbacks, such as toxicity after photolysis. Their comparably large size and the targeting chemistry holds particular difficulties.

3.1.3 Photobleaching

Photobleaching is the irreversible loss of fluorescence of a fluorescent molecule by permanent photochemical alteration of its chemical structure. It occurs after a stochastically distributed number of absorption and emission cycles. When a fluorophore gets excited by a laser photon, it is able to interact non-specifically with other surrounding molecules, which can lead to chemical changes and, thus, photobleaching. At the same time, cleavage of covalent bonds possibly results in loss of fluorescence. In fluorescence microscopy, photobleaching is an important aspect to consider, when interpreting the obtained data. As bleaching occurs during imaging, it can be responsible for significant changes of the results and impair their quality. For single particle tracking experiments, for example, photostability of the fluorophore is crucial. It increases both the total number and the length of observed trajectories. In some cases, e.g. in FRAP or TOCCSL experiments, photobleaching is an essential part of the technique since fast bleaching of a specified area is required.

The time until photobleaching of an excited fluorescent molecule can vary from milliseconds for fluorescent proteins up to hundreds of seconds or longer for quantum dots. In order to minimize photobleaching in an experiment, the exposure time and intensity can be decreased; however, this results in a lower signal-to-noise-ratio. The photobleaching behavior of many fluorophores has been studied extensively in solution as well as in biological environments. For simplicity, many studies use single-exponential curves in order to describe the photobleaching characteristics, which has proven to be a good description for photobleaching in solution. Significant deviations, however, seem to occur between the bleaching behavior of fluorescent molecules in solution and in the plasma membrane of live cells. Amongst others, the chemical interaction between the fluorophore and other molecules of the membrane and the presence of molecular oxygen are affecting the bleaching characteristics and demand new models [42]. In order to ade-

quately describe the photobleaching behavior in a cellular environment, the random orientation of the fluorophores has to be taken into account, which is leading to non-exponential bleaching. In addition, chemical modifications and attachment of fluorophores to distinct conjugation sites are possible reasons for a multi-exponential bleaching process [43].

3.1.4 Fluorescence intensity of a fluorophore

Typically within nanoseconds after excitation (= fluorescence lifetime), a fluorophore emits a photon. In single molecule microscopy, the fluorescence intensity or brightness of fluorescent molecules and the probability density function are of particular importance. The exact number of photons, that are released as a response to the excitation, is governed by stochastic processes. According to [44], the probability density function for the fluorescence intensity of a single emitter is well approximated by a log-normal distribution. In addition to the intrinsic stochastic nature of the process, defocusing as well as slight differences in the distance of the fluorophore from the glass surface in TIR configuration can lead to variations in intensity. Aberrations, variations in the pixel quantum efficiency in the (EM)CCD camera and variations in the excitation intensity are other influences leading to fluctuations in the detected signal. For identification of oligomeric states in a TOCCSL experiment, the knowledge of the pdf of the single molecule fluorescence intensity is crucial (see Sec. 2.5). Since it depends on multiple factors like the particular sample chemistry, optical properties of the setup and more, it has to be determined experimentally.

3.1.5 Total internal reflection fluorescence microscopy

When probing the plasma membrane with a conventional fluorescence microscope, the signals are usually overlaid by intracellular background fluorescence. Total Internal Reflection Fluorescence Microscopy (TIRFM) is a technique for exclusively exciting the molecules near the glass slide, i.e. at the cell surface of attached cells. It is an especially useful tool for single molecule detection. It was first described as a method for selective surface illumination [45] and then further developed by *Daniel Axelrod* for cell experiments [46].

TIRFM makes use of the phenomenon of total internal reflection. Excitation light is reflected at the interface between the microscope slide and the aqueous specimen. Fluorescent molecules are therefore only excited in a layer of around 100 nm distance to the glass surface by

the evanescent field of the reflected light beam. Hence, the cytosolic background signal is significantly reduced, resulting in a better signal-to-noise ratio and a better localization precision of the fluorescent molecules. TIRFM is well-suited for investigating the cell membrane and their constituents as well as dynamic processes at or close to the membrane like protein-protein interactions or endocytosis. It is particularly used for single particle tracking and super-resolution techniques.

When an electromagnetic wave encounters the interface between two media of different refractive indices, either reflection, refraction or both occurs. For isotropic media, Snell's law describes the relation between the angle of incidence θ_1 and refraction θ_2 and the two refractive indices of the media n_1 and n_2 by

$$n_1 \sin\theta_1 = n_2 \sin\theta_2 \ . \tag{3}$$

Total internal reflection occurs only if an electromagnetic wave - propagating in a medium with n_1 - encounters a medium with $n_2 < n_1$. A condition for the angle of incidence can be derived from Snell's law in order to define the regime for TIR configuration.
Assuming $n_2 > n_1$, total reflection is represented by an angle of refraction of $\theta_2 = 90$ (Fig. 6B) leading to

$$n_1 \sin\theta_c = n_2 \ . \tag{4}$$

Hence, the critical angle $\theta_1 = \theta_c$ can be expressed as

$$\theta_c = \sin^{-1}\frac{n_2}{n_1} \ . \tag{5}$$

Following this classical law, the wave is totally reflected for all incident angles greater than the critical angle θ_c (Fig. 6C). For some photons there is certainly a non-zero probability to be refracted. The predominant fraction of the wave, however, will be internally reflected. At the interface of the two media, the electromagnetic wave penetrates the medium of lower refractive index up to a depth of 100-200 nm. The penetration depth depends on the particular wave length, the angle of incidence of the incoming photons and the refractive indices. This part of the wave is termed *evanescent wave* or *field*. It propagates perpendicular to the interface and is responsible for the excitation of fluorophores in TIRFM. The intensity of the evanescent wave

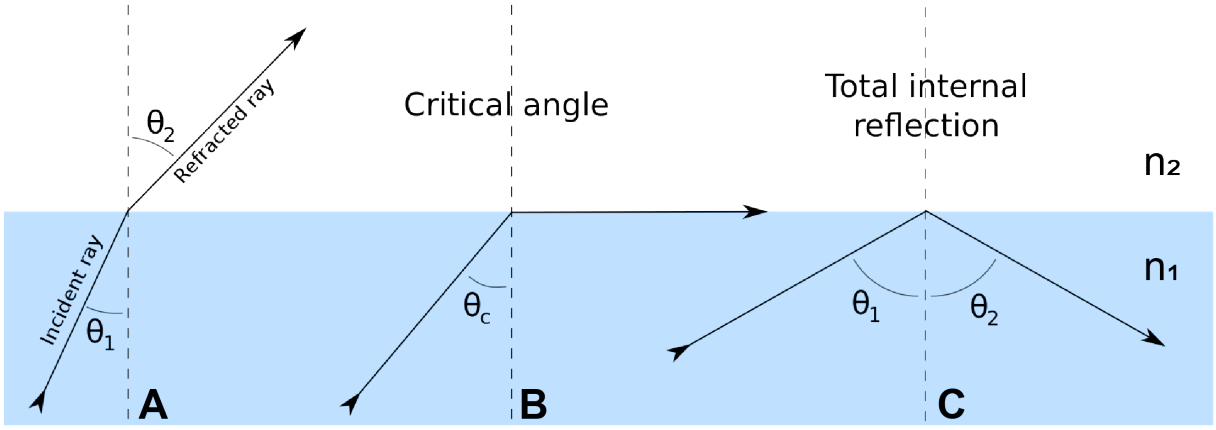

Figure 6: Schematic figure of refraction and reflection of light at the interface of two media with refractive indices $n_2 < n_1$. **A** Refraction of light for a subcritical incidence angle θ_1. **B** Refraction at critical angle θ_c. **C** Total internal reflection of a light beam with incidence angle $\theta_1 > \theta_c$. Figure adapted under free license from en.wikipedia.org/wiki/Total_internal_reflection.

follows an exponential decay

$$I(z) = I_0 e^{-\frac{z}{d}}, \tag{6}$$

where z denotes the distance from the interface and d the characteristic penetration depth, which is given by

$$d = \frac{\lambda}{4\pi}(n_1^2 \cdot \sin^2 \alpha - n_2^2)^{-\frac{1}{2}} \tag{7}$$

for an incident angle α and wavelength λ. By increasing the incidence angle to values greater than the critical angle, the penetration depth of the evanescent field is decreased, yielding a further reduction of intracellular background.

TIRFM can be realized by two different approaches based on an inverted microscope geometry, which are the objective lens method (Cis-TIRFM) and the prism method (Trans-TIRFM). The prism method is less established due to geometrical constraints on specimen manipulation and imaging through the bulk of the specimen. In the objective lens method (Fig. 7), the laser light is introduced through an objective of a high numerical aperture (NA), usually an oil immersion objective. The numerical aperture represents the range of possible illumination angles and is given by $NA = n \sin \theta$, where n denotes the refractive index of the surrounding medium and θ half the angular aperture of the objective lens. Oil immersion objectives can be used to ensure that total internal reflection solely occurs at the interface between glass slide and sample. In order to avoid refraction at the glass slide, the immersion oil should approximately have the same refractive index as the glass. The refractive index of the cytosol is typically around

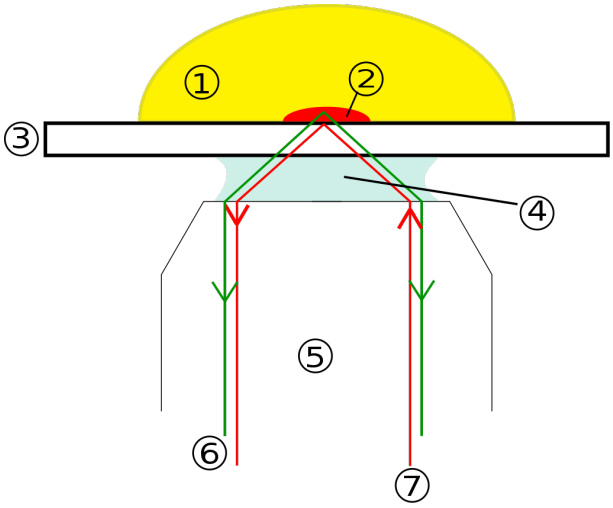

Figure 7: Schematic illustration of the objective lens method for TIRF microscopy. **(1)** Specimen **(2)** Evanescent wave range **(3)** Cover slip **(4)** Immersion oil **(5)** Objective **(6)** Emission beam **(7)** Excitation beam. Figure adapted under free license from de.wikipedia.org/wiki/Interne_Totalreflexionsfluoreszenzmikroskopie.

$n_{cytosol} = 1.38$. For total internal reflection at a cell surface, which is closely attached to the glass substrate, the numerical aperture is therefore restricted to values greater than 1.38.

3.1.6 Single molecule microscopy

Whereas ensemble techniques only yield averaged values of a parameter for a whole ensemble of fluorescent molecules, single molecule microscopy reveals further information on biological systems (structure, dynamics, stoichiometry, etc.). Single molecule microscopy allows for determining the composition of heterogeneous populations as well as localizing the positions of individual fluorophores in the subpixel regime. Furthermore it is possible to unravel correlations of various molecular parameters by measuring them simultaneously. For example, mobility can be related to the oligomerization state to obtain a better understanding of the diffusion process [47].

3.1.7 Single molecule localization

An imaged point-like source of light is represented by its point spread function (PSF), typically an Airy pattern. The resolution of two adjacent fluorescent molecules is limited by diffraction (see Sec. 3.2.1). A single molecule, however, can be localized below the diffraction limit of light microscopy by analyzing its PSF. The localization precision of a single emitter is essentially limited by the number of emitted photons and the finite pixel size. Precise localization can be

done by deconvolution of the blurred signal with its PSF. For reasons of practicability, the PSF is usually approximated by a two-dimensional Gaussian function since it represents a good fit for the Airy disc and the overall decreasing intensity towards the radial direction. The coordinates of a single emitter can be determined by identifying the center of the Gaussian fit. Thus, the localization precision depends on the quality of the approximation and, hence, the quality of the signal. A simple estimation for the localization precision is given by the standard deviation σ of the PSF (Gaussian fit) and the number of collected photons N:

$$\langle \Delta x^2 \rangle = \sigma^2 N. \tag{8}$$

Another theoretical limit for the two-dimensional localization precision was suggested by *Thompson et al.* in [48], where the uncertainty in each dimension is given by

$$\langle \Delta x^2 \rangle = \frac{\sigma^2 + a^2/12}{N} + \frac{8\pi\sigma^4 b^2}{a^2 N^2}. \tag{9}$$

Here, a denotes the finite pixel size and b the background noise, which is assumed to be constant across the region of the spot being analyzed. According to [49], Eq. 9 underestimates error bars systematically and to such an extent that it violates the information limit when applied to their experimental data. An adjusted estimate for the variance of the displacement is given by

$$\langle \Delta x^2 \rangle = \frac{\sigma_a^2}{N}\left(\frac{16}{9} + \frac{8\pi\sigma_a^2 b^2}{a^2 N}\right), \tag{10}$$

where essentially the factor 16/9 compensates for errors occuring due to Eq. 9.

Due to pixelation the precision is limited. As the signal spreads over several pixels and is fitted by a Gaussian function, the localization precision, nevertheless, enters the subpixel regime. Optimization of the imaging system such as optimal focus, correction for aberrations, high numerical aperture or maximal incidence angle for TIR illumination are increasing the number of detected photons and minimizing the standard deviation of the fit. Furthermore, not only the properties of the optical system but the brightness of the detected fluorophore as well is crucial for a maximum localization precision. Movement of the fluorophore (or the whole cell) during illumination also reduces the localization precision.

3.2 Diffraction

Whenever a wave interacts with an object, e.g. a slit, diffraction occurs in different forms. A beam of light, for instance, appears to bend around an obstacle into its geometric shadow, which is not directly illuminated by the beam. The phenomenon of diffraction, however, is not restricted to light, but comprises all types of waves, i.e. acoustic waves, particle waves, etc. The effects are usually most pronounced when the object's dimensions are roughly comparable to the wavelength of the propagating wave.

3.2.1 Diffraction of a point source and the resolution limit of light microscopy

In 1873, Ernst Abbe first described the required distance of two lines of a grating in order to be resolvable. For condensed light with a wavelength λ propagating through a medium with refractive index n, the resolution limit is described by

$$d = \frac{\lambda}{2n \sin \alpha} = \frac{\lambda}{2NA}, \tag{11}$$

where NA denotes the numerical aperture and α half the angular aperture of the objective. For optical microscopy, the diffracted image of a point-like light source is of particular interest. A point source is never imaged as a point, but rather as a smeared out spot. As mentioned before, the response of an imaging system, e.g. a microscope, to a point source is described by the *point spread function*. Diffraction occurs at the margins of the objective lens or at the edges of a circular aperture at the back focal plane of the lens. As a result, a point is imaged as a diffraction pattern termed *Airy pattern*, after Sir George Airy (1801-92). The Airy pattern consists of a bright central region, known as the Airy disk and concentric rings of a periodic intensity scheme with minima and maxima (see Fig. 8). The center is called the zeroth maximum of the pattern followed by a radial series of minima and maxima. The characteristics of the pattern, especially the size of the disk, are depending on the wavelength of the emitted light and the angular aperture of the lens.

According to the so-called Rayleigh criterion, two distinct adjacent point sources of light are defined as resolvable, if the distance between the two zeroth maxima of the Airy patterns is at least equal or greater than the distance between the zeroth maximum and the first minimum of

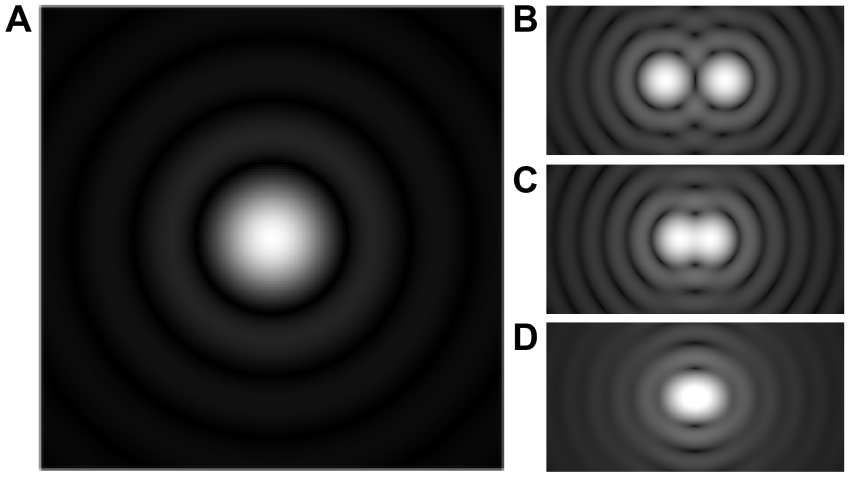

Figure 8: **A** Computer generated image of an Airy pattern. **B** Airy patterns of two resolvable adjacent point-like light sources. **C** Visualization of the Rayleigh criterion for two adjacent point-like light sources. The center of one Airy disc is located in the first minimum of the other Airy disc. **D** Image of two point-like light sources, which are not resolvable according to the Rayleigh criterion. Figures adapted under free license from en.wikipedia.org/wiki/Airy_disk and en.wikipedia.org/wiki/Angular_resolution#Explanation

one Airy pattern. This is, without derivation, described by

$$\sin\theta \approx 1.22\frac{\lambda}{D} \ , \tag{12}$$

where θ denotes the angular resolution, λ the wavelength of the emitted light and D the diameter of the angular aperture of the lens. The factor 1.22 is derived from a calculation of the position of the first dark circular ring (first minimum) surrounding the central Airy disc of the diffraction pattern. In other words, the radius d of the diffraction spot for a self-luminous point of light in the image plane is given by

$$d \approx 1.22\frac{\lambda}{2NA} \tag{13}$$

with the numerical aperture $NA = n\sin\theta$.

Irrespective of diffraction, lens aberrations are another limiting factor for the resolution. When the resolution of an imaging system is limited by diffraction rather than aberrations or scattered light, it is called *diffraction-limited*. Obtaining information on the structure of an object is only possible, if the dimensions of the structures are greater than the resolution limit. [50]

3.2.2 Diffraction at a slit aperture

Since a rectangular slit aperture is used to confine the illuminated and photobleached area in a TOCCSL experiment, diffraction should be considered as impairment of the photobleaching process. Commonly, the Fresnel number N_F is used to classify the employed physics depending on the width of slit D, the wavelength λ and the distance to the observation plane d

$$N_F = \frac{(D/2)^2}{\lambda \cdot d}. \tag{14}$$

The diffraction of light at a rectangular aperture in the far-field approximation can be described by the Fraunhofer diffraction integral. It can be applied for $N_F \ll 1$. According to [51], the intensity I of a light beam with wavenumber k diffracted at a rectangular aperture with side lengths $2a$ and $2b$, is given by the solution of the diffraction integral as

$$I(x,y) \propto I_0 \left(\frac{\sin kax}{ax}\right)^2 \left(\frac{\sin kby}{kby}\right)^2 . \tag{15}$$

This approximation is applicable, if the side lengths of the aperture are roughly comparable to the wavelength of the diffracted light. To avoid far-field diffraction leading to an inhomogeneous excitation profile in experiments, the aperture should be placed in a way that the width of the slit exceeds this regime. The typical side length of the aperture in the TOCCSL setup, that was also used in this work, is a few millimeters. Assuming a width of 5 mm and a wavelength of 500 nm, according to Eq. 14, the distance to the observation plane would have to be greater than 25 m to obtain a value of $N_F < 1$, which represents the limit to Fraunhofer diffraction. Hence, the Fresnel number N_F for the TOCCSL setup is much greater than 1 and, therefore, near-field diffraction effects are predominant. These effects are described by the Fresnel approximation of the diffraction integral, which only is analytically solvable for the simplest geometrical forms. A typical laser intensity profile, used for a TOCCSL experiment, can be seen in Fig. 9. It is characterized by an oscillating plateau bordered by a rapidly decreasing edge region. The gradient in the laser profile is relevant for TOCCSL simulations since the photobleaching probability for an illuminated fluorophore strongly depends on the laser intensity at its position.

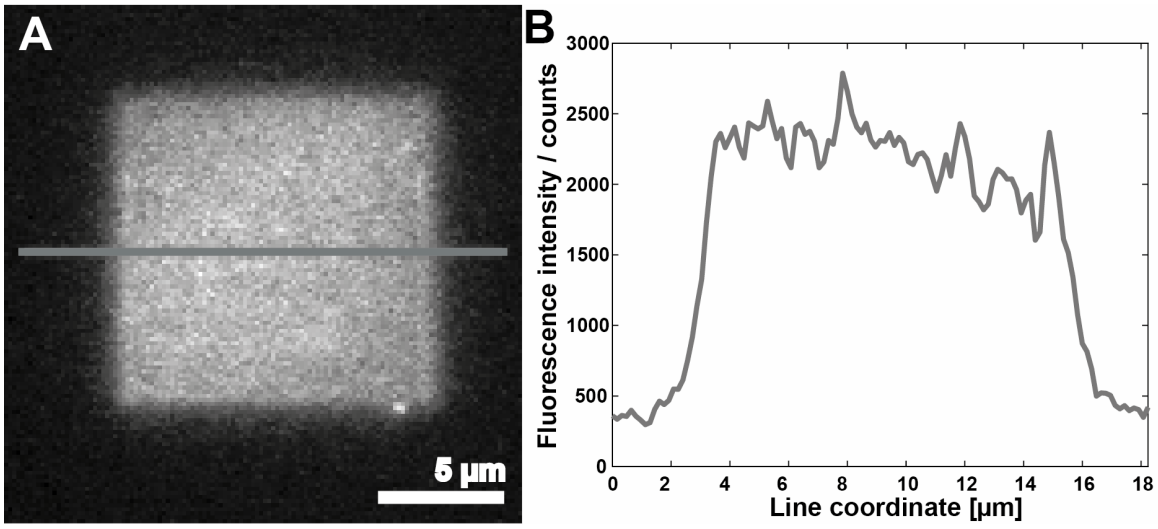

Figure 9: **A** Homogeneous sample of GPI-anchored mGFP in the plasma membrane of a CHO cell, illuminated in TIR configuration. **B** The fluorescence signal along the solid line represents the lateral laser intensity profile influenced by diffraction at the rectangular aperture.

3.3 Diffusion

In a cell, molecules are in constant rotational and translational motion propelled by thermal energy. They repeatedly undergo collisions with other molecules and therefore move in a random fashion, called *Brownian motion*. Diffusion processes of an admixture in a medium are described by Fick's laws. Fick's first law connects the diffusional flux $\vec{J}$ with the concentration of the admixture ϕ by

$$\vec{J} = -D\nabla\phi, \tag{16}$$

where D denotes the diffusion coefficient. The driving force for diffusion in this equation is given by the concentration gradient. Fick's second law can be derived by inserting the continuity equation $\frac{\partial\rho}{\partial t} + \nabla \cdot \vec{J} = 0$ into Eq. 16, yielding a partial differential equation:

$$\frac{\partial\phi}{\partial t} = D\Delta\phi \tag{17}$$

Here, Δ denotes the Laplacian operator. Eq. 17 shows the spatial evolution of the concentration over time caused by diffusional motion, which is characterized by the diffusion coefficient D. In a more general case, D is not constant, but as a function of ϕ represented by a symmetric,

positive definite matrix. Thereby the diffusion equation describes anisotropic diffusion:

$$\frac{\partial \phi(\mathbf{r},t)}{\partial t} = \sum_{i=1}^{3}\sum_{j=1}^{3} \frac{\partial}{\partial x_i}\left[D_{ij}(\phi,\mathbf{r}) \frac{\partial \phi(\mathbf{r},t)}{\partial x_j} \right] \tag{18}$$

Due to randomness, the movement of a single freely diffusing particle with $D = const.$ can only be described in terms of probabilities. Rephrasing Eq. 17 yields

$$\frac{\partial p(\vec{r},t)}{\partial t} = D\left[\frac{\partial^2}{\partial x^2} + \frac{\partial^2}{\partial y^2} + \frac{\partial^2}{\partial z^2} \right] p(\vec{r},t) \ . \tag{19}$$

The one-dimensional solution of Eq. 19 for the starting condition $p(x,t) = \delta(x)\delta(t)$ is given by

$$p(x,t)dx = \frac{1}{\sqrt{4\pi D t}} e^{-\frac{x^2}{4Dt}} dx \ , \tag{20}$$

where $p(x,t)dx$ represents the probability to find a particle at the time t in the interval $[x, x+dx]$. The probability is given by a gaussian function with a mean value at the starting position (in this case: $\langle x \rangle = 0$) and a variance $\sigma^2 = 2Dt$.

For lateral diffusion in the plasma membrane, further considerations will be restricted to two dimensions and a constant diffusion coefficient D (Eq. 17). In this case the two-dimensional solution is given by the product of the individual distributions in x- and y-direction

$$p(x,y,t)dxdy = \frac{1}{4\pi D t} \ e^{-\frac{x^2+y^2}{4Dt}} dx \ dy \ . \tag{21}$$

3.3.1 Trajectory analysis

An important quantity of diffusional processes is the so-called *mean squared displacement* (MSD). For random diffusion, it is given by the second moment of the probability distribution for the particle's position. In an n-dimensional space, it is given by

$$\left\langle \vec{r}^2 \right\rangle = \int_{-\infty}^{\infty} \vec{r}^2 \cdot p(\vec{r},t) d\vec{r} = 2nDt \ . \tag{22}$$

The MSD depicts the average of squared distances, that particles have covered after the time t. It can be calculated as mean value of many steps of a single particle trajectory (average over time) or as mean value of displacements for a single time step of an ensemble of particles

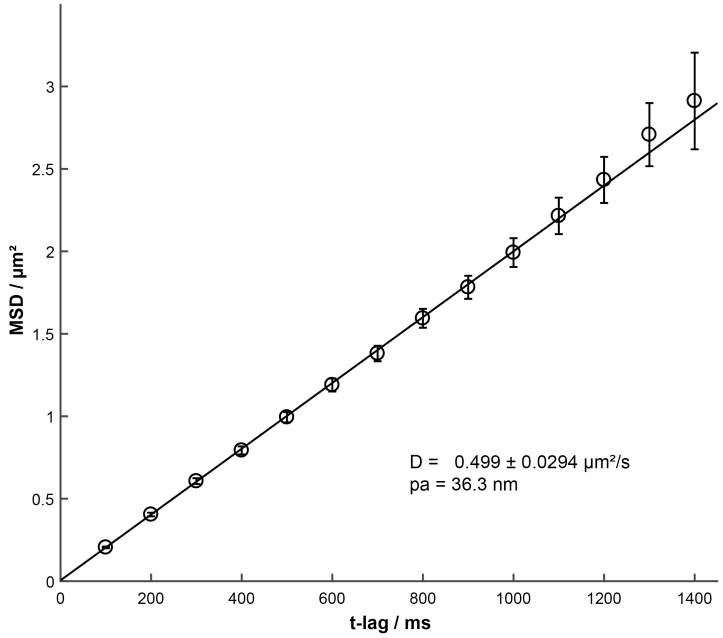

Figure 10: MSD plot for simulated randomly diffusing particles. 100 trajectories with a diffusion coefficient $D = 0.5\ \mu\text{m}^2/\text{s}$, a trajectory length of 15 steps and a time lag of 100 ms were simulated. The error of the calculated MSD is more pronounced for greater time lags since the number of available displacements for the MSD calculation is decreasing. The diffusion coefficient D was determined by fitting the first two data points by a linear function according to Eq. 24. The distance from the origin to the fit on the y-axis yields the positional accuracy (pa).

(ensemble average). In an ergodic system both values are equal.

In Single Particle Tracking (SPT) experiments, a commonly used method to analyze the trajectories is based on an MSD plot (Fig. 10), where the MSD is determined for varying time lags and plotted versus time t (Fig. 10). Experimentally, the first time lag is given by the time between two consecutive images. In general, the mean squared displacement $\langle r^2 \rangle$ for the nth time lag of a single trajectory is given by

$$\langle r^2 \rangle_{n\Delta t} = \frac{\sum_{i=1}^{N-n+1} r_{i,n\Delta t}^2}{N-n+1}, \tag{23}$$

where n = 1, 2, 3,..., N. According to that, the MSD for a certain time lag Δt is calculated by all possible displacements between two data points of a trajectory, that are separated by the time Δt. Usually, the displacements of many measured trajectories are taken into account for the calculation of the MSD.

There are various suggestions for the characterization of motion via the MSD versus time lag curve [6, 52, 53]. A quadratic dependence on t, where $\langle r^2 \rangle \propto t^2$, indicates active transport. A proportionality of $\langle r^2 \rangle \propto t^\alpha$, where $\alpha < 1$, indicates confined diffusion and $\langle r^2 \rangle = R^2(1 - e^{-\frac{4Dt}{R}})$ describes anomalous subdiffusion within a circle with radius R. A linear MSD plot represents free (random) diffusion, which is in two dimensions given by

$$\langle r^2 \rangle = 4Dt + 4\sigma^2, \tag{24}$$

where D depicts the diffusion coefficient. Due to the limited position accuracy of a measurement, the additional term of $4\sigma^2$ has to be introduced, where σ denotes the position accuracy [54]. Experimental data of randomly diffusing particles can be analyzed via MSD plot and fitted by Eq. 24 in order to determine the diffusion coefficient D and the positional accuracy σ.

3.3.2 Size-dependent lateral mobility of membrane proteins

The lateral diffusion of membrane proteins plays a major role in regulating protein-protein interactions. In 1975, *Saffman* and *Delbrück* suggested a model [55] that links the diffusion coefficient with the inclusion radius of membrane-bound proteins by taking the viscosity of the liquid membrane μ and the surrounding aqueous phase μ' into account. According to their model, the translational diffusion coefficient D_T for a cylindrical object with radius a is given by

$$D_T = \frac{k_B T}{4\pi\mu h}\left(\ln\frac{\mu h}{\mu' a} - \gamma\right) . \tag{25}$$

Here, h denotes the thickness of the membrane and γ is the Euler-Mascheroni constant. This formula shows only a weak dependence of D_T on the inclusion radius a. The Saffman-Delbrück (SD) model has proven to be valid in a limited range of viscosities and inclusion sizes. *Hughes et. al* [56] extended the model to intermediate values of membrane viscosity and arbitrary inclusion sizes, which led to a more accurate approximation but also to a rise in computational effort due to the required numerical solution of integral equations. Inconsistent results with the SD model have given rise for other models, which account for further influences. For example, local deformations of the membrane - caused by protein-lipid interactions - could result in deviations of the SD model [57]. For several integral proteins it was shown that the diffusion coefficient is more strongly dependent on the protein dimensions [58] than originally described

by the Saffman-Delbrück model. A dependence on the inclusion radius of a^{-1} instead of $ln(a)$ has been suggested. Although some studies have confirmed the suggested model [59, 60], these dependencies have not always been observed [34]. It seems, however, as if the correlation between particle size and mobility, in general, has not been investigated very extensively.

3.4 Influences on a TOCCSL experiment and sources of error

In a TOCCSL experiment, possible sources of error can lead to both in under- and overestimation of certain oligomeric states and, therefore, the outcome of an experiment can be biased in different directions. Concerning the Monte Carlo simulations developed in this work, it is essential to consider the individual influencing factors separately in order to characterize and quantify the effects on the experimental outcome.

3.4.1 Incomplete maturation of fluorescent dyes

Transfected cells are commonly used in experiments, where a fluorescent protein is fused to the target protein. This holds the possibility of incomplete labelling due to incomplete maturation or misfolding of fluorescent proteins [21]. Thus, a fraction of target proteins is in a dark state and not accessible in the experiment. The degree of mGFP, for instance, has been estimated in previous studies to be around 85 % [21, 36]. The same effects possibly occur using labeled antibodies since there is the possibility of underlabeling of the antibody, e.g. due to steric hinderance, or a poor labeling efficiency due to inaccessible epitopes. Unspecific binding of a fluorophore would also have an influence on the results. In contrast, the usage of polyclonal antibodies leads to a broadening of the fluorescence intensity pdf but is not considered as an error source. The developed simulations, however, do not account for a reduced maturation rate or labeling efficiency since - assuming the knowledge of labeling efficiency - it is straightforward to calculate the impact on the final result for any given value.

3.4.2 Incomplete photobleaching

The photobleaching process is a substantial part of the TOCCSL method. Ideally, photobleaching occurs instantaneously as response to an infinitely short laser pulse of high intensity, causing all fluorophores within a well-defined illuminated region to bleach irreversibly. There are two major reasons, why photobleaching can not be conducted in such an optimal way.

I. Finite bleaching time

Due to limited laser intensity and bleaching probabilities, an extended laser pulse is required to bleach all particles within the aperture. Typically, bleaching times t_{bleach} of a few hundred milliseconds are employed. During that time, the fluorescent molecules are diffusing in and out of the photobleached region confined by the aperture. In case of oligomers, the diffusion causes incomplete bleaching of clusters. The bleaching probability for individual fluorophores is assumed to be independent of cluster size. When detected at the end of the recovery time, incompletely bleached aggregates appear as oligomers of lower order. For example, a dimer initially carrying two active fluorophores could be detected as a monomer if one fluorophore remains fluorescent after photobleaching. In a TOCCSL experiment, this effect could result in an overestimation of monomeric and lower order oligomeric states, in general, and an underestimation of oligomers of higher order.

If the bleaching time is simply too short, some molecules within the central region of the illuminated area will remain fluorescent (Fig. 17B). These molecules are very likely to be partially bleached higher order multimers since monomers or lower order oligomers would - with a high probability - be completely bleached. This may also favor the underestimation of higher order oligomers. However, recording a control image after photobleaching enables to adjust the bleaching time in order to prevent incomplete bleaching in the central region of the illuminated area.

II. Diffraction

Diffraction of the laser beam at the aperture (see Sec. 3.2.2) leads to an inhomogeneous laser intensity profile in the XY-plane of the specimen. In particular a slit or rectangular aperture results in an intensity gradient at the edge of the illuminated region. Hence, the probability for a fluorophore near the edge of the aperture to be bleached is decreased due to the reduced laser intensity. As a result, fluorophores may remain fluorescent within the edge zone or again, clusters may be incompletely bleached, enabling the possibility of falsely detecting a lower order oligomer.

On the one hand, diffusion during photobleaching leads to an edge zone with increased concentration of incompletely bleached particles (see Fig. 17C-D). On the other hand, due to diffraction, the reduced laser intensity near the edge of the confined area additionally increases the width

of the edge zone and the concentration of partially bleached molecules.

3.4.3 Mobility differences

Reduced mobility of membrane proteins with increasing size (inclusion radius) as suggested by the Saffman-Delbrück model and theories beyond that (see Sec.3.3.2) would lead to an overestimation of fractions of a low degree of oligomerization. After the specified recovery time, the likelihood of high order oligomer fractions to enter the central region of the photobleached area, where brightness analysis is performed, is reduced due to a decreased diffusion coefficient compared to the monomeric fraction.

3.4.4 False colocalizations

Two detected signals, represented by their PSFs, are resolvable if they fulfill the Rayleigh criterion (see Sec. 3.2.1). In many cases, two overlaying signals beyond the diffraction limit can be rejected and excluded for further analysis by analyzing the quality fit of the 2D Gaussian function, in particular the full width at half maximum (FWHM). However, if the signals of two randomly encountered molecules are too close to each other and exclusion of analysis fails, they will be detected as a single molecule. Therefore, the stoichiometry of these particles is determined by the convolution of the two individual PSFs. In the present work, this will be referred to as *false positive* or *false colocalization*.

The detection of false colocalizations contributes to the overestimation of aggregates with higher subunit counts. The distance threshold for two separate signals to be detected as a single aggregate and thus the extent of influence on the outcome of an experiment, depends on the resolution of the microscopy setup, the emission wavelength of the fluorophore as well as the quality of fitting algorithms.

4 Methods

All simulations were developed and performed on a standard personal computer using MATLAB (R2016b, The MathWorks Inc., Natick, MA).

4.1 Simulation of particle trajectories

Brownian motion is mathematically described by a Wiener process (after *Norbert Wiener*). It is a continuous-time stochastic process, where the increments for each time step are Gaussian distributed and independent of past values of the trajectory (Markovian). The Wiener process can be constructed by a random walk in the limit of infinitely small steps (*Donsker's theorem*). Thus, the simulation of diffusion can be approximated by a random walk using a stationary independent increment for the calculation of the new coordinates. This is feasible if a sufficiently dense time-grid is used. In this work, the simulation is implemented as a Gaussian random walk. The individual step size is randomly drawn from a Gaussian distribution, which is more "exact" than the random walk with a stationary increment. Off-lattice simulations are performed, i.e. the coordinates of the trajectories are not assigned to discrete values of a grid. The core of the simulation is the calculation of the step size Δr for every discrete time step Δt. The probability distribution for a single step can be derived from the solution of Fick's second law, Eq. 17. The solution in 2D is given by Eq. 21, which constitutes the probability of a particle to remain after the time t in the spatial interval $[x,\ x+dx]$ and $[y,\ y+dy]$.
The transformation $dxdy = rdrd\varphi$ with the Jacobian determinant $J = r$ yields the two-dimensional solution in polar coordinates:

$$p(r, \Delta t)\ drd\varphi = \frac{1}{4D\Delta t}\ r\ e^{-\frac{r^2}{4D\Delta t}}\ drd\varphi. \tag{26}$$

The probability distribution is independent of φ and therefore equally distributed over all angles and symmetric around the point of origin. The dependence of the step size distribution is presented in Fig. 11 for a Gaussian random walk in one and two dimensions.

In order to simulate 2D Brownian motion, it is more convenient to overlay two one-dimensional random walks in x- and y-direction instead of generating random numbers from the distribution in polar coordinates (Eq. 26). The separate steps for both coordinates Δx and Δy are randomly drawn from the Gaussian probability distribution (Eq. 20) with a variance $\sigma^2 = 2Dt$,

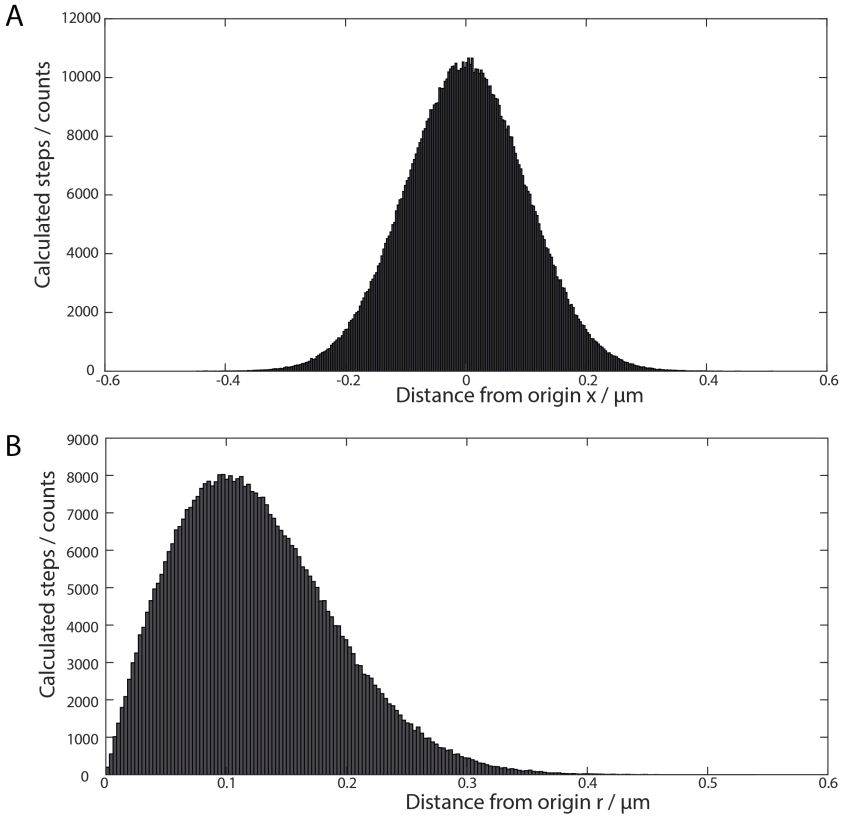

Figure 11: **A** Histogram of separately calculated step sizes in 1D for a TOCCSL simulation. The diffusion is simulated by combination of two 1D-Gaussian random walks in x- and y-direction. **B** Histogram of calculated step sizes $r = \sqrt{x^2 + y^2}$ in 2D for a TOCCSL simulation corresponding to the radial distribution in polar coordinates in Eq. 26. The angles φ are uniformly distributed (not shown here).

that is centered around the origin ($\mu = 0$). This is can easily be done with standard routines generating Gaussian distributed random numbers (e.g. here: built-in *normrnd*-function in MATLAB). After the random numbers Δx and Δy are drawn from the probability distribution, new coordinates are assigned to a particle for a single step:

$$x_{new} = x_{old} + \Delta x$$

$$y_{new} = y_{old} + \Delta y$$

The step length in polar coordinates Δr of the particle in 2D can be calculated as $\Delta r = \sqrt{x^2 + y^2}$, whereas φ follows a uniform distribution over all angles.

For this work, diffusion of typically around 100.000 particles is simulated. First, the starting position for each particle is assigned in cartesian coordinates. These coordinates x and y are

randomly drawn from a uniform distribution, typically on the interval $[0, 35]$, resulting in a total area of $A = 35 \times 35 = 1225\ \mu m^2$ (for the particular simulation parameter sets, please refer to AppendixA). Subsequently the step sizes in x- and y-direction are randomly drawn as described. This is done for the total number of steps, that are required for all particles in the simulation. In order to provide for the coordinates of a particle, the cumulative sum of the starting position and the individual steps is calculated, yielding the particle's trajectory over the course of the simulation.

According to these calculations, the trajectories are determined irrespective of the interval initially confining the starting positions. In order to preserve the particle surface density, reproduce the finite size of a cell and thus provide for a finite reservoir of particles, boundary conditions are applied. Whenever a particle's trajectory exceeds the boarder of the predefined rectangular area, it is set to the opposite side of the area by adding or subtracting the respective side length. The coordinates of the diffusing particles are thereby confined to the specified interval.

The coordinates at every calculated time point for a whole simulation run are stored in a multidimensional array. Later, additional entries of the array are assigned to the oligomeric and the fluorescent state of each particle. The exact coordinates are of importance for the photobleaching process, where the bleaching probability depends on the location within the aperture. They are as well required for the analysis of the oligomeric state after the recovery time. It is assumed that the photobleaching of a fluorescent molecule does not influence its diffusional behavior. Hence, the trajectories of all particles can be determined beforehand and the photobleaching process is calculated in a subsequent, separate simulation step.

4.2 Assignment of oligomeric and fluorescent states

The oligomeric state is assigned to the particles in an additional entry in the multidimensional array containing the trajectory coordinates. A perfect labeling efficiency as well as a degree of labeling of 1 is assumed for simplicity. Thus, the oligomeric state is equal to the initial number of active (non-bleached) fluorophores attached to the particle. The fluorescent state is again assigned to each particle in an additional entry of the array. While the oligomeric state is not changed during the simulation, the initial number of active fluorophores is altered during the simulated photobleaching process. For simplicity, dissociation and recombination of aggregates

is not taken into account.

In general, arbitrary distributions of oligomeric fractions can be assigned to the particles as an input parameter (see Sec. 4.7). For the majority of the simulations that were performed in the course of this work, the initial oligomeric distribution was chosen in a way that the effects of the investigated phenomena on the results are most pronounced in order to facilitate their interpretation.

4.3 Account for mobility differences

The code allows for the simulation of molecular populations with distinct diffusion coefficients. Arbitrary distributions of oligomeric states N can additionally be assigned with distinct values for $D = D(N)$ as input parameters. The previously described calculation steps are done separately for the particles of the respective population. The step size distribution for each species changes according to the variance of the 1D normal distribution $\sigma^2 = 2\mathbf{D(N)}t$. This enables the investigation of the influence of mobility differences between molecules with differing numbers of subunits.

4.4 Photobleaching probability

In order to characterize the photobleaching behavior of fluorophores in a TOCCSL experiment, photobleaching curves were measured in live cells. As a representative cellular system that was already studied in [34, 38, 61], glycosylphosphatidylinositol(GPI)-anchored monomeric green fluorescent protein (mGFP) in the plasma membrane of Chinese hamster ovary (CHO) cells was used for measurements. Cells were prepared and treated as described in [34]. Cells with a homogeneous distribution of fluorescence were selected by eye for the experiment. For excitation, an optically pumped solid-state laser (Coherent, Sapphire) with a wavelength of 488 nm was used. After pre-bleaching in epi-illumination mode for reduction of the cytosolic background, a sequence of 700 images with an illumination time of 1 ms and a time-lag of 7 ms between consecutive images was recorded in TIRF configuration. The measurements were taken with a laser intensity of roughly 5 kW/cm^2 on the specimen plane, which is typically used for photobleaching of mGFP in TOCCSL experiments. The integrated brightness over time of a manually selected homogeneous ROI was then fitted via linear least squares by a two-component

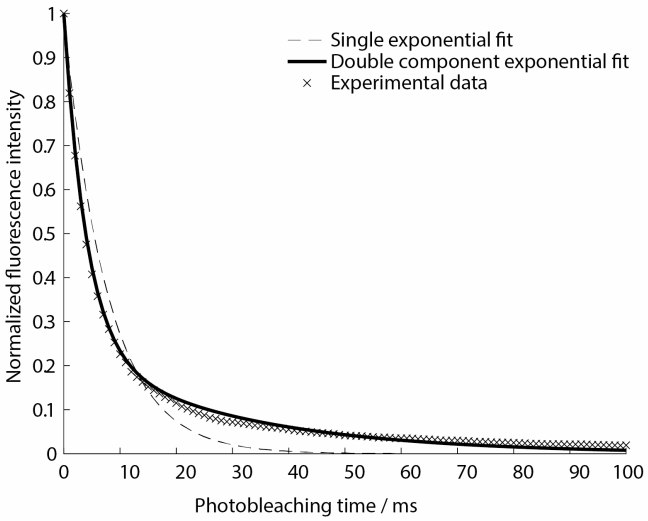

Figure 12: Photobleaching Curve. The curve was recorded for GPI-mGFP in CHO cells with a laser intensity of ~ 5 kW/cm^2 and fitted by a single component exponential function as well as a double component exponential function (Eq. 27). The single exponential fit shows significant deviations from experimental data. For calculation of bleaching probabilities, the fit parameters from the two-component exponential function were used.

exponential function

$$f(t) = Ae^{-\alpha t} + Be^{-\beta t} + C. \tag{27}$$

α and β denote the so-called bleaching parameters, A and B are the weights of the two fit components and C represents the background signal. The background can be subtracted for the following calculations since the bleaching probability only depends on the bleaching parameters and respective weights. The fit was done for 6 different cells and the mean values of the fit parameters were used for further calculations. The exponential fit yields a bleaching probability $p(t)$ for a fluorescent molecule to be irreversibly photobleached after the illumination time t

$$p_{bleach}(t) = 1 - (A\ e^{-\alpha t} + B\ e^{-\beta t}), \tag{28}$$

where A and B are normalized, such that $A + B = 1$.

It is noted that the bleaching parameters α and β have been determined specifically for mGFP in CHO cells and for the laser intensity of $\sim$5 kW/cm^2. They serve as representative values for the simulations. In order to characterize another biological system or experimental configuration, it is necessary to determine the photobleaching behavior of the utilized fluorophores.

4.4.1 Influence of diffracted laser beam

Photobleaching, in general, is dependent on illumination intensity, which is consistent with Eq. 28, where $\alpha = \alpha(I)$ and $\beta = \beta(I)$ are functions of the laser intensity I at the specimen plane. As for the recording of photobleaching curves in Sec. 4.4, live CHO-cells stably expressing GPI-mGFP were used to characterize the laser intensity profile influenced by diffraction. The aperture was adjusted such that a square with a side length of around 12 μm is illuminated. According to Fig. 9, the lateral brightness profile was analyzed, yielding the same characteristics in x- and y-direction. The intensity gradient at the edge of the laser profile in one dimension was approximated by Gaussian functions and the oscillating part by a constant plateau. The relative laser intensity with respect to the maximum value at the plateau is then specified for the absolute value of the distance x to the center of the illuminated region by

$$\begin{aligned} X(|x|) &= 1 && \text{for } |x| \leq \frac{d_{ap}}{2} - d_{edge} \\ \textit{and } X(|x|) &= \exp\left(-\frac{(|x| - (d_{ap}/2 - d_{edge}))^2}{\sigma^2}\right) && \text{for } |x| > \frac{d_{ap}}{2} - d_{edge}, \end{aligned}$$

where d_{ap} denotes the aperture's side length, which is equal to the illuminated area, and d_{edge} the width of the intensity gradient, which is part of the illuminated area. The value for d_{edge} was estimated according to the fit of the measured intensity profile and was fixed at $d_{edge} = 1$ for the simulations in this work. In order to obtain a two-dimensional intensity profile, the relative intensities in x- and y-direction - $X(x)$ and $Y(y)$ - are multiplied with each other, yielding a normalized 2D intensity profile $I(x, y) = X(x) \cdot Y(y)$. It is then used to calculate the corresponding photobleaching probability for a single time step Δt for a particle with coordinates x and y inside the illuminated region

$$p_{bleach}(x, y, \Delta t) = 1 - (A\ e^{\alpha I(x,y)\Delta t} + B\ e^{\beta I(x,y)\Delta t}). \tag{29}$$

A, B, α and β have been determined as described in the previous section. The 2D photobleaching probability for a squared aperture is shown in Fig. 13. Hence, in case of a diffracted laser profile, the bleaching probability is a function of the particle's coordinates.

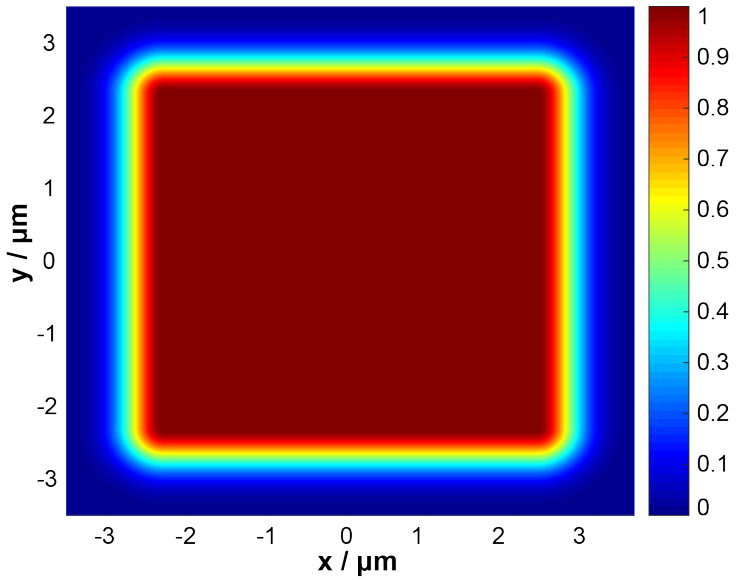

Figure 13: Normalized calculated bleaching probability for the illuminated region during a TOCCSL experiment with a squared aperture of side length 7 μm. Due to diffraction at the aperture, the probability is a function of the coordinates within the confined region and was calculated according to the approximated laser intensity profile (Eq.29). The plateau in the central region with the maximum value (normalized to 1) is surrounded by the edge region with decreasing bleaching probability.

4.5 Simulation of the photobleaching process

Since photobleaching is a stochastic process, the determination, whether a particle is bleached or remaining fluorescent, is calculated by a Monte Carlo method. After calculation of the bleaching probability on the interval from zero to one, a uniformly distributed random number on the same interval is generated and compared to the previously calculated probability. If the number is less than or equal to the probability of photobleaching, the particle is bleached. In case of oligomers, this is done independently for all active fluorophores assigned to the particle. If the fluorescent state of a particle is changed, the new fluorescent state is assigned to the residual part of the particle's trajectory. Simulations of photobleaching are done for two different scenarios:

(i) The first case is based on the idealized laser profile without diffraction effects. A coordinate-independent bleaching probability inside the illuminated region, which is given by Eq. 28, is assumed. Furthermore it is constant for each single time step Δt. Outside the aperture, the probability is considered zero. Hence, the probability for a particle to be photobleached after t_{bleach} arises from the total time $t_{total} = n_{total} \cdot \Delta t$, that the particle has remained within the illuminated region during t_{bleach}. The total number of discrete time steps n_{total} is determined

by analyzing the particle's trajectory. The bleaching probability is then given by

$$p_{bleach}(n_{total}) = 1 - (A\ e^{\alpha\ n_{total}\ \Delta t} + B\ e^{\beta\ n_{total}\ \Delta t}). \tag{30}$$

For the uniform laser profile, the probability $p_{bleach}(n)$ is pre-calculated for all possible numbers of time steps $n = 1, 2, 3, ..., (t_{bleach}/\Delta t)$. By doing so, the required probability can easily be recalled and repeated calculation of the same probability is prevented, hence allowing for faster computation.

(ii) In the second case, the photobleaching probability is calculated for all particles within the illuminated ROI and individually for every time step during the total photobleaching time t_{bleach}. At every time point during t_{bleach} the coordinates of all particles are queried. For the particles inside the illuminated area, the probability is determined as a function of the illumination intensity at the exact coordinates according to Eq. 29. At the end of every photobleaching step, the current fluorescent state is assigned to the residual part of the particle's trajectory. Thus, the new state constitutes the basis for the next photobleaching step.

4.6 Data analysis

After completion of the photobleaching process, the particles of the corresponding TOCCSL image at the end of the recovery time are analyzed. A priori all particles within the illuminated region are considered for further analysis. In order to account for limited resolution, only particles, which are separated from all other particles at least by the threshold distance d_{res}, typically around 300 nm, are evaluated. Furthermore, only N_{inner} innermost particles - with N_{inner} being an input parameter - within a ROI centered at the origin are analyzed (full line in Fig. 14). The smallest possible ROI with a shape similar to the aperture geometry, i.e. squared or rectangular, which exclusively contains the requested number of particles, is determined. This allows for exclusion of particles in the outer region of the bleached area, that are in fact separated from all other particles by at least d_{res} but surrounded by a large number of fluorescent molecules. Due to the high surface density in this surrounding, these molecules are inaccessible for analysis in a real experiment.

Subsequently, for the N_{inner} particles within the ROI, the distances to all other particles

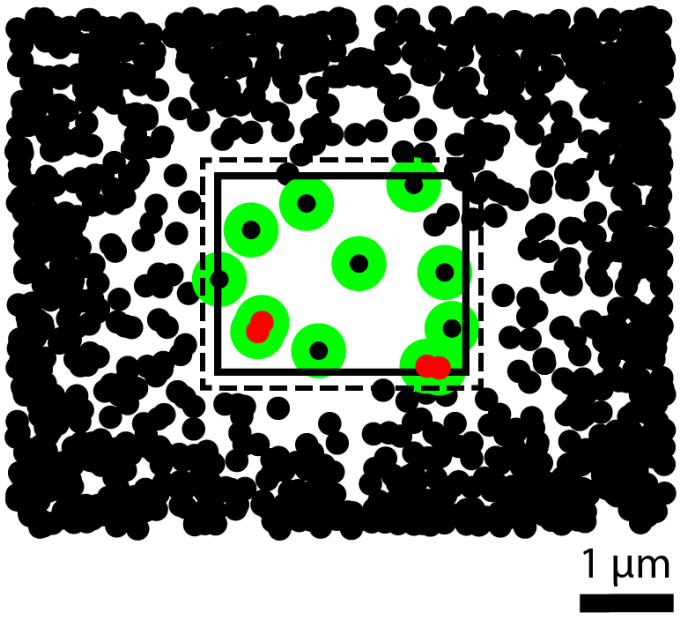

Figure 14: Illustration of computer simulated particles in a typical situation used for data analysis (TOCCSL image). According to Sec. 4.6 the 15 innermost particles within a rectangular ROI (full line) are used for analysis. For the 15 innermost particles, the distances to all particles within an enlarged concentric, similar ROI (dashed line) accounting for the resolution limit, are calculated. The black spots encircled in green are well-separated by the specified resolution threshold d_{res} and therefore considered as resolvable particles for further analysis. If the distance between two particles is smaller than a specified colocalization threshold d_{FP}, while the distances to all other particles are greater than d_{res}, they are tagged and analyzed as false colocalization (red spots).

within an enlarged concentric and similar rectangle around this ROI (dashed line in Fig. 14), whose side lengths are increased by d_{res} in each direction. This accounts for the inability to resolve certain particles near the edge of the analyzed ROI due to the vicinity of fluorescent particles located slightly outside of the ROI but within a radius d_{res}. If all calculated distances are greater than the threshold d_{res}, the particle is considered for analysis. If at least one other particle is closer than d_{res} both particles are excluded from further analysis unless false positive detection of aggregates due to random encounters is taken into account. Then, further conditions have to be met as described in the next section.

4.6.1 Account for false colocalizations

Taking the possibility into account, that two adjacent particles could falsely be detected as a single multimer, further conditions have to be defined. Two or more particles are considered as a false positive, if the distance between them is smaller than a certain distance d_{FP} and at the

same time, the distances of the individual particles to all other particles are greater than the resolution threshold d_{res}. The same integer is assigned to the particles of the same colocalization as a tag in the array A containing the information on the particles within the analysis ROI at the end of recovery. The tag integer allows for identification of the individual particles as part of the same aggregate at a later time point. In order to determine the detected degree of oligomerization (according to the brightness) for a particular aggregate, the numbers of active fluorophores n_j of j individual particles are summed up yielding $n_{tot} = \sum_j n_j$ with n_{tot} being the total number of active fluorophores for a false positive. The value $n_{tot} = 2$ corresponds to a dimer, $n_{tot} = 3$ to a trimer, etc. The total number of colocalizations contributing to a particular N-mer fraction (all particles with $n_{tot} = N$), i.e. the number of false dimers, trimers, etc., is then counted and stored as an additional row in the analysis matrix as described in Sec. 4.6.2. An analyis situation for one simulation is shown in Fig. 14.

4.6.2 Determination of oligomeric fractions

All particles that are considered as resolvable are counted according to their oligomerization state N and their number of active fluorophores A. The number of resolvable particles of each oligomeric fraction is then stored in the analysis matrix M_{ij} of the form $dim(M_{ij}) = (n_{nmer} + 1) \times n_{nmer}$. The first index i corresponds to the assigned oligomerization state N and the second index j to the number of active flourophores A for each particle. With exception of the last row, the matrix is of the form $M(N, A)$. Thus, all "detected" monomers are stored in the first entry of the first column M(1,1). The total number of dimers with two active fluorophores is stored in the matrix element M(2,2), whereas the number of partially bleached dimers with only one active fluorophore is assigned to M(2,1) etc. An additional row is added for false positives, where the number of false monomers, dimers, trimers,... is indicated in the first, second, third,... column, respectively.

For the simulations discussed in this work, typically a few hundred runs with equal parameters are performed. Every single run yields a result matrix M that is stored. After completion of the simulation, all matrices are summed up element by element to obtain the total number of particles for each fraction. In order to calculate the oligomeric fraction with N subunits, all entries of the N^{th} column are summed up and divided by the total number of analyzed particles (sum of all entries of M). If false positives are not taken into account, the last row is simply

left out for the calculation.

4.7 Simulation parameters

This section overviews the most important input parameters to run a TOCCSL simulation. The following parameters are those accessible via graphical user interface. In order to run a simulation, all of these parameters have to be assigned correctly. A flow chart of the simulation is given by Fig. 15.

t_bleach

t_bleach defines the photobleaching time in milliseconds. For all time steps during *t_bleach*, the bleaching probability is calculated for the particles that are located within the illuminated region.

laser_shape 'uniform', 'diffraction', 'ideal'

Two different types of modeled laser intensity profiles are implemented as described in Sec. 4.5. These are affecting the photobleaching probability and thus the extent of incomplete bleaching. The parameter $'ideal'$ specifies ideal bleaching of fluorophores meaning instantaneous photobleaching of all fluorescent particles within the illuminated region.

t_recovery

t_recovery specifies the recovery time in seconds. It defines the time after photobleaching until the analysis of the particles is executed. During *t_recovery*, non-bleached particles randomly diffuse into the bleached area.

n_nmer

n_nmer defines the highest degree of oligomerization. It can be an arbitrary integer number. If, for example, $n\_nmer = 1$ is chosen, only monomers are simulated, $n\_nmer = 2$ means that monomers and dimers are simulated etc. The distribution of the individual fractions is defined by the variable *fraction*.

fraction

The distribution of the oligomeric fractions (values between 0 and 1) are assigned to the array *fraction*. The $\boldsymbol{N}$th entry defines the $\boldsymbol{N}$mer fraction. Since the entries are relative fractions, the sum of the individual values must add up to 1. The array dimension must be equal to *n_nmer*. Example: $n\_nmer = 3$, $fraction = [0.6\ 0.3\ 0.1]$

D

D is an array, that contains the diffusion coefficients of the individual oligomeric fractions in $\mu m^2/s$. In D, mobility differences can be assigned to different species. The $\boldsymbol{N}$th entry stands for the diffusion coefficient of the $\boldsymbol{N}$mer fraction. The array dimension must be equal to *n_nmer*.

density

The variable *density* specifies the overall surface density in particles per μm^2. The number of simulated particles is then calculated according to the specified grid size and the respective oligomeric state is assigned according to the distribution specified in *fraction*. In order to obtain the desired surface density in *fluorophores* per μm^2, the distribution of nmer fractions has to be taken into account.

roi_x, roi_y

roi_x and *roi_y* specify the side lengths of the rectangular aperture in μm.

stepno_second

stepno_second defines the number of computational steps, that are done per simulated second. For example, assuming a bleaching time of 500 ms and a recovery time of 1.5 seconds, a value of $stepno\_second = 300$ results in 600 simulated steps in total. The accuracy of results depends strongly on this parameter as the results converge only for a relatively high value (see Sec. 5.1).

res_limit

res_limit specifies the experimental resolution limit for two adjacent particles. If the distance between two neighboring particles is less than *res_limit*, both particles are excluded from further analysis with the exception of the analysis of false colocalizations (see *fp_limit*).

fp_limit

If the distance between the two adjacent particles is smaller than fp_limit and at the same time, the distances of both particles to all other particles in their proximity are greater than the resolution threshold res_limit, the particles are regarded as a false positive.

innermost_particles

innermost_particles specifies the number of the most central particles within a smallest possible ROI, that are considered for analysis.

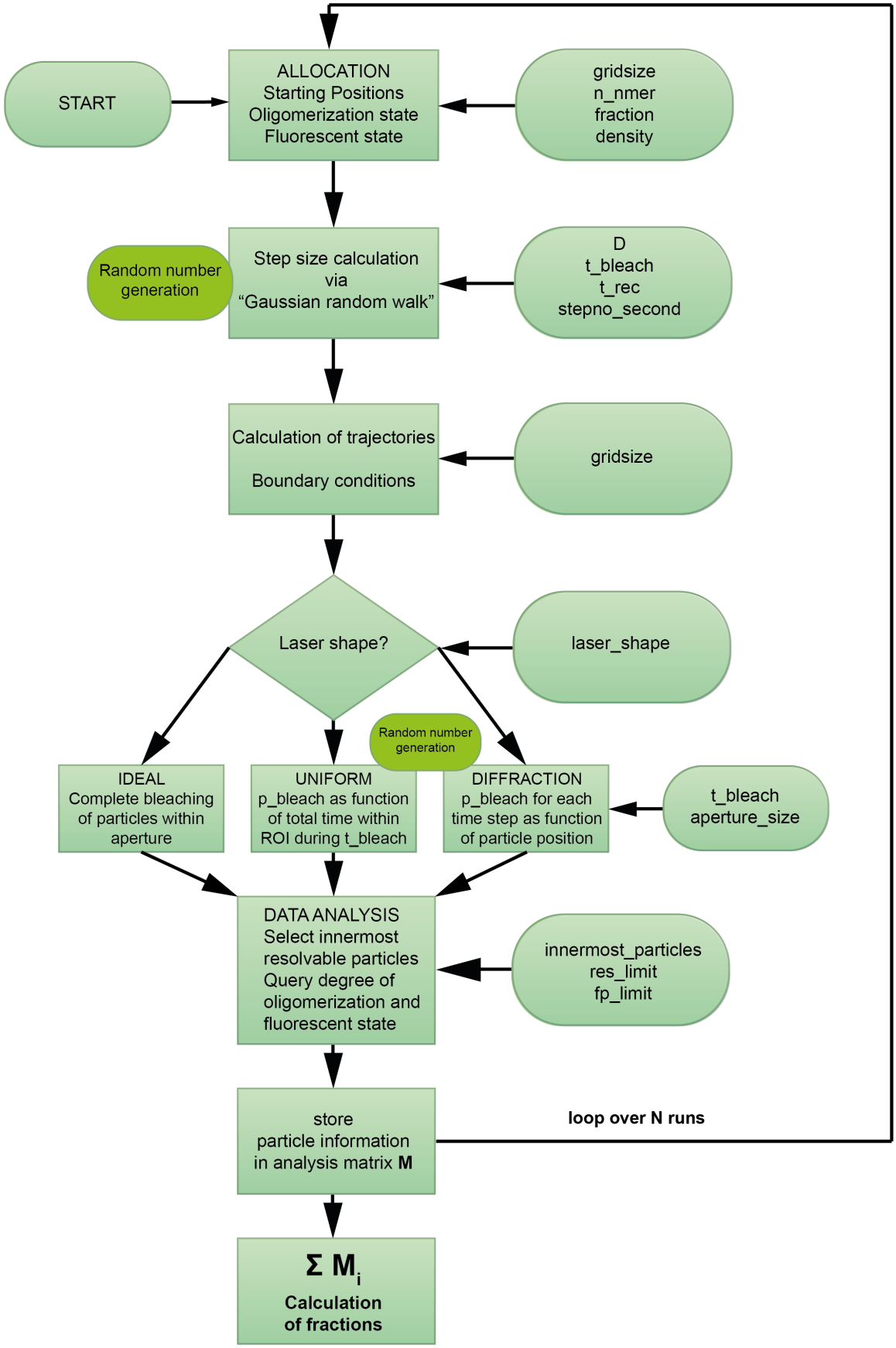

Figure 15: Flow Chart for a TOCCSL simulation. The requested input parameters are shown to the right of the simulation steps. Typically a few hundred runs (N>100) are performed for the simulation of an experiment with a particular parameter set. The result matrices M_i of the individual runs are stored. After completion of all runs, the resulting oligomeric fractions are calculated.

5 Results

5.1 Convergence study for simulated photobleaching

The discretization of time restricts the algorithm to a finite number of simulated time steps. One of the simulation's key parts, namely the photobleaching process, is affected by the density of the time grid since the probability for bleaching is calculated according to the time steps that a particle remains within the illuminated area. An increase in simulated steps per time unit allows for more particles to diffuse in and out of the illuminated region, leading to an increase in both completely and partially bleached molecules. Thus, a sufficiently small time grid is crucial for the outcome and the quality of the simulation. An increase in time steps, however, will raise the computational effort disproportionally since it increases the number of computational operations in several parts of the simulation. In order to quantify the effects of the chosen time grid on the results and to ensure that a sufficient number of steps is used for further investigations, simulations with a varying number of steps were carried out. A TOCCSL experiment with an initial population of 100 % dimers with a diffusion coefficient of $D = 0.5\ \frac{\mu m^2}{s}$ was simulated with a bleaching time of $t_{bleach} = 500$ ms and a recovery time of $t_{recovery} = 1.5$s (for the complete set of input parameters, refer to Appendix A). The simulated steps per second were varied from 1 to 500. In Fig. 16 the resulting dimer fraction and the total number of partially bleached dimers is shown as function of the number of steps. Both figures are referring to the same effect. With an increasing number of time steps, the number of partially bleached molecules is increased as well, hence the detected dimer fraction is reduced. The curves converge to a constant value for high numbers of simulated steps. A sufficiently high number should be used as simulation parameter to rule out major influences due to time discretization. In order to limit the processing time for further simulations, 300 simulated steps per second were chosen as a compromise because it appears to be the lower boundary of the constant part of the curve. Of note, the simulation of diffusion is not as much affected by the dimension of the time grid since it is based on the quasi-exact calculation of the step size by Gaussian distributed random numbers.

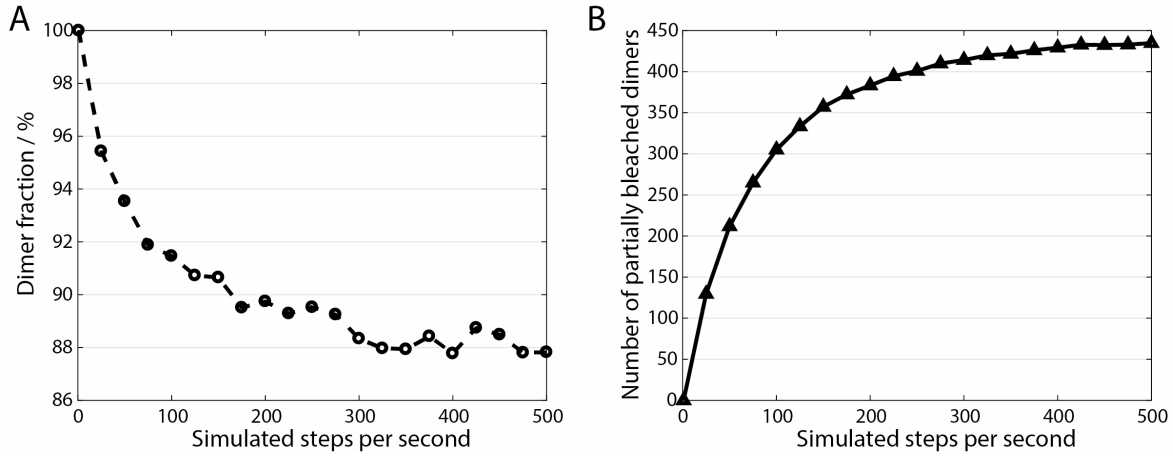

Figure 16: Simulation of a TOCCSL experiment with an initial population of 100 % dimers. The apparent dimer fraction (**A**) and the total number of partially bleached dimers (**B**) is shown for a varying number of simulated steps per second. Due to the discretization of time, the full extent of incomplete photobleaching only becomes visible for a large number of steps.

5.2 Incomplete photobleaching

5.2.1 Influence of photobleaching time

A priori it is not intuitively clear, how the photobleaching time affects the outcome of an experiment. In particular the consequences of long bleaching pulses are of interest as partial bleaching of oligomers is essentially based on Brownian motion during the time of excitation.

In Fig. 17 the simulated outcome of a TOCCSL experiment for a homogeneous population of 100 % dimers as a function of the photobleaching time is presented. Assuming $\rho = 100$ molecules/μm^2, a diffusion constant $D = 0.5$ μm^2/s and a recovery time $t_{rec} = 1.5$ s, the photobleaching time was varied between 0 and 700 ms.

Simulations with oligomeric molecules show a distinct region of high concentration of partially bleached molecules near the edges of the bleached area (Fig. 17C-D). Compared to a uniform laser intensity profile, the effects are more pronounced for the case of a diffracted laser profile.

The results reveal that, in general, a longer bleaching time yields more accurate results. The curve is saturating towards a longer bleaching time. Only minor changes in the experimental outcome occur in the saturated regime for bleaching times greater than 300 ms. Short photobleaching does not only lead to incomplete bleaching at the edge but in the center of the illuminated region as well (see Fig. 17B); therefore it causes a lower apparent dimer fraction. The downside of a longer bleaching time, however, is an increased depletion of fluorescent molecules and a decrease in surface density, respectively. Thus, the number of experiments, that can be

conducted in the very same cell is reduced, leading to an increased experimental effort in order to obtain the same amount of data. It is thus suggested that the photobleaching time is chosen at the bottom of the curve's plateau, where the target region is bleached sufficiently, but overall depletion is kept on a relatively low level.

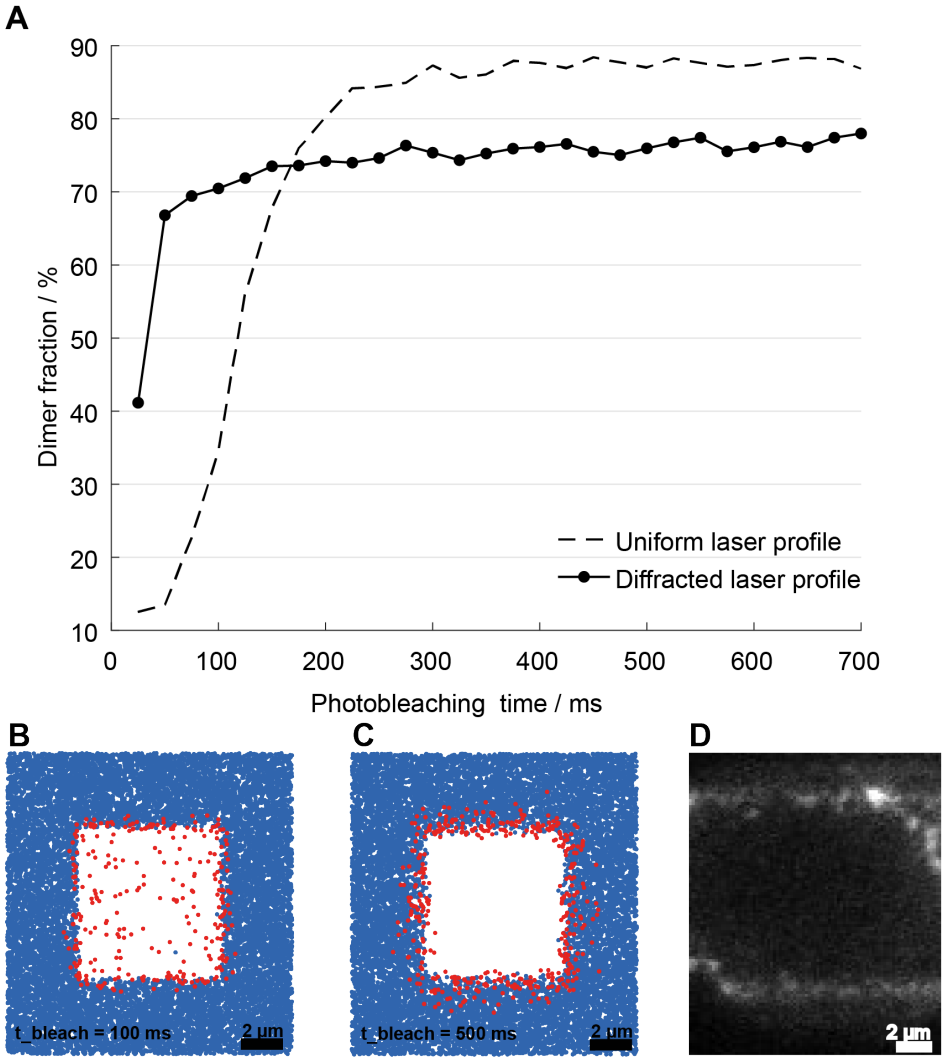

Figure 17: **A** Resulting dimer fraction (original fraction: 100 %) for varying photobleaching time in a simulated TOCCSL experiment. **B-C** Simulated post-bleach situation for 100 % dimers. Fully fluorescent dimers are shown as blue spots and partially bleached dimers as red spots. In panel B, the bleaching time $t_{bleach} = 100$ ms is too short in order to completely bleach the region within the aperture. Panel C shows a pronounced edge zone with a high concentration of partially bleached dimers for a typical experimental bleaching time $t_{bleach} = 500$ ms. **D** Recorded image of GPI-mGFP in the plasma membrane of CHO cells after 500 ms of photobleaching with a laser intensity of ~ 5 kW/cm^2.

5.2.2 Influence of recovery time

The choice of recovery time depends on the mobility of the target protein, the initial surface density and the size of the photobleached region. It is essential to understand how the recovery time affects the detection of partially bleached clusters. Simulations were done to investigate whether the very onset of the recovery or a more advanced time point is preferable for recording and analyzing an image. A population of 100 % dimers, a diffusion constant of $D = 0.5\ \mu\text{m}^2/\text{s}$ and a photobleaching time of $t_{bleach} = 500$ ms was used as parameter set. The recovery time t_{rec} was varied between 0 and 3.6 seconds. For $t_{rec} > 3.6$ s, the high surface density in the analyzed region already prevents the possibility to resolve individual particles. The results in Fig. 18 are shown for the uniform as well as the diffracted laser intensity profile. Both reveal a higher dimer fraction, hence more accurate measurements for longer recovery times. After a short recovery time, most of the analyzed particles are still located in the vicinity of the edge region. The edge region, however, contains a high concentration of partially bleached particles (Fig. 18B). Thus it is more likely to detect partially bleached molecules resulting in a higher experimental monomer fraction and an accordingly lower dimer fraction for short t_{rec}.

If the maximal recovery time is applied, the analyzed molecules are located close to the center of the ROI (Fig. 18C). The high surface density in the outer regions does not allow for resolving single molecules. The dimer fraction increases significantly with the recovery time. Less incompletely bleached particles are detected. In this regard, the distribution of incompletely bleached particles over time is discussed in the next section (Sec. 5.2.3). In Fig. 18A, however, statistical fluctuations of the resulting dimer fraction are evident for longer t_{rec}. Less particles are resolvable as the surface density of fluorescent particles in the bleached region is continuously increased during the recovery time. Hence, the drawback of a long recovery time is low statistics.

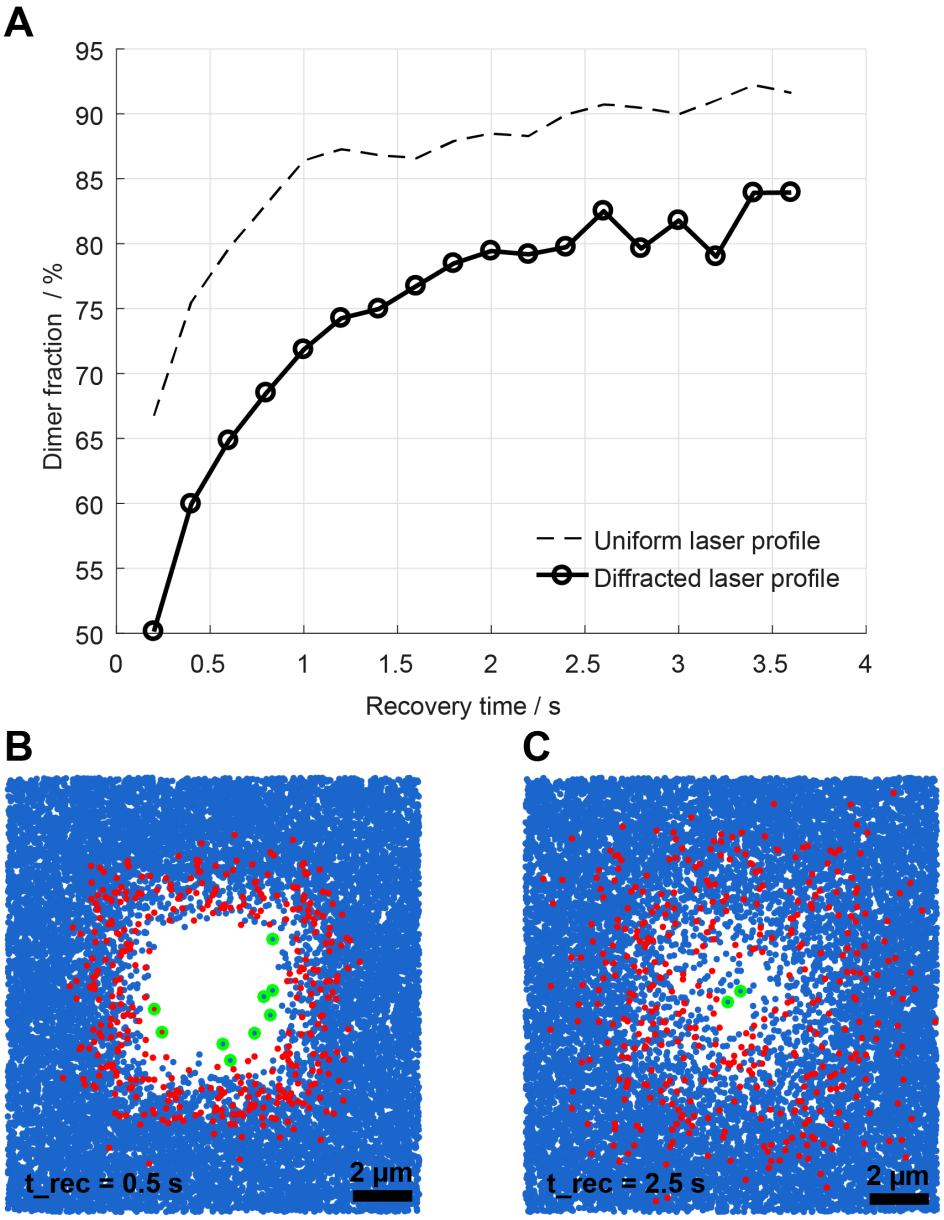

Figure 18: **A** Resulting dimer fraction (original fraction: 100 %) for varying recovery time in a simulated TOCCSL experiment. **B-C** Simulated TOCCSL analysis images of an original fraction of 100 % dimers for $t_{rec} = 0.5$ s (panel B) and for $t_{rec} = 2.5$ s (panel C). Fully fluorescent dimers are represented as blue spots, partially bleached molecules as red spots. Particles satisfying the diffraction-limit and, hence, considered for analysis, are encircled in green. After a short t_{rec}, particles are analyzed near the edge of the photobleached region, which contains a large number of incompletely bleached particles. After an extended t_{rec}, the concentration of incompletely bleached molecules is diluted within the analyzed area near the center.

5.2.3 Distribution of incompletely bleached particles

The TOCCSL approach strongly depends on the reduction of surface density of fluorescent molecules in the photobleached and analyzed region. The surface density profile after ideal photobleaching along the x-axis for a slit aperture with infinite extension along the y-axis is given by [35]

$$\rho(x,t) = \rho_0 \left[1 - \frac{1}{2}\,\mathrm{erf}\left(\frac{x + dx/2}{\sqrt{4Dt_{rec}}}\right) + \frac{1}{2}\,\mathrm{erf}\left(\frac{x - dx/2}{\sqrt{4Dt_{rec}}}\right)\right], \tag{31}$$

where dx is the width of the slit, D the diffusion coefficient and t_{rec} the recovery time. With regard to Eq. 31 the distribution of non-bleached particles after photobleaching was examined via simulations. These were performed with 100 % dimers, $\rho_{surface} = 100$ dimers/μm^2, $D = 0.5$ μm^2/s, $t_{bleach} = 500$ ms and a squared aperture with a side length of 8 μm. Photobleaching was simulated with the diffracted laser profile. Due to the squared aperture geometry, the surface density ρ along concentric squares around the origin is constant. In order to obtain the surface density as a function of the distance x to the center, $\rho(x)$ was determined in stripes with a width of 100 nm between concentric squares (see Fig. 19C). This yields a "local" surface density $\rho(x)$ defined along the x- or y-axis as a function of the distance to the center x. In this context, the distribution of incompletely bleached molecules during a TOCCSL experiment is of particular interest since Eq. 31 does not account for incomplete bleaching.

Fig. 19A shows the surface density of fluorescent molecules after photobleaching and roughly reflects Eq. 31. Rather small deviations result from the fact that the equation was derived for an aperture with infinite extension along one dimension. Furthermore ideal photobleaching and, hence, a sharp interface between the bleached and non-bleached particles as starting condition was assumed.

The distribution of incompletely bleached dimers after photobleaching is shown in Fig. 19B. As the particles are spreading across the membrane, the concentration of partially bleached particles is diluted toward the center of the ROI. The ratio of non-bleached particles to partially bleached particles increases within the analyzed ROI with increasing values of t_{rec}. Hence, the probability of detecting a partially bleached particle after a long t_{rec} within the central part of the the photobleached area is small compared to the probability within the edge region after a short t_{rec}.

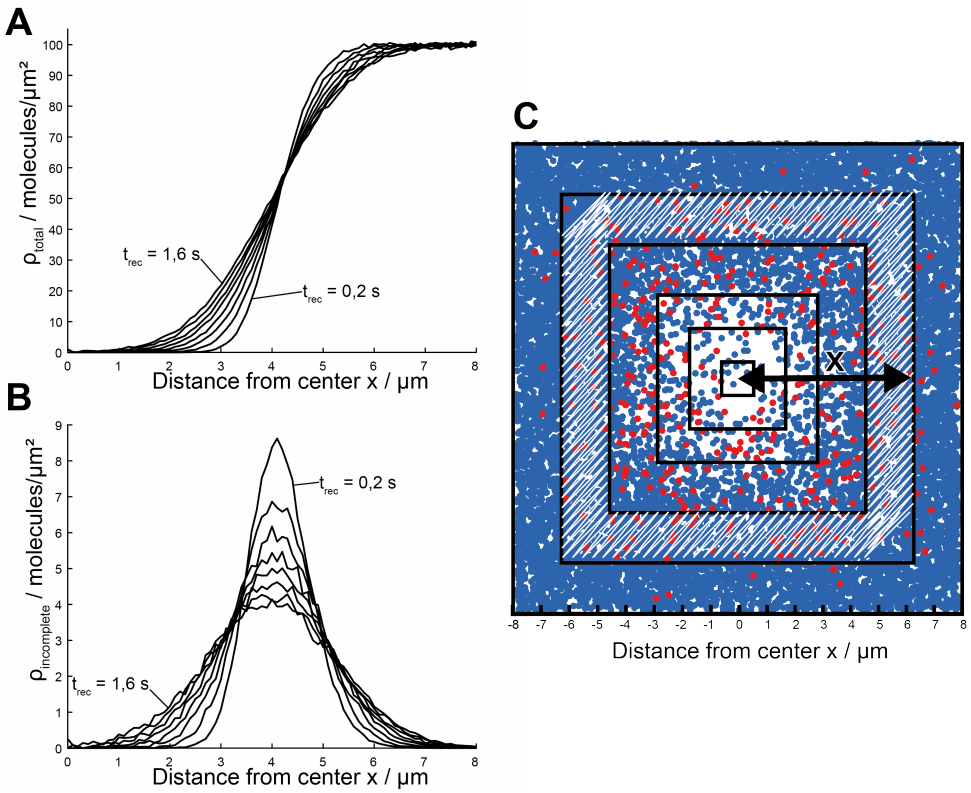

Figure 19: Calculation of local surface density in a TOCCSL experiment. Simulations were done for a pure dimer population, a squared aperture with a side length of 8 μm and varying recovery times from 0.2 to 1.6s. The initial surface density was assumed to be 100 molecules per μm^2 and $D = 0.5\ \mu m^2/s$. After photobleaching, fluorescent particles enter the bleached region. The surface density of all fluorescent particles is shown in panel **A** as a function of the distance to the center of the bleached region along the x- (or y-)axis. The edge of the aperture is located at x = 4 μm. The curves approximately reflect Eq. 19. Panel **B** shows the surface density of incompletely bleached dimers. The local surface density was calculated, according to panel **C**, within stripes of 100 nm width between concentric squares. The particle positions of 100 simulation runs were used for the calculation of ρ.

5.2.4 Influence of diffusion coefficient

The following simulations were performed to quantify the impact of the target molecule's mobility on incomplete photobleaching. A homogeneous population of 100 % dimers with $\rho_{surface} = 100$ dimers/μm^2 and a photobleaching time of $t_{bleach} = 500$ ms was simulated. The diffusion constant D was varied from 0.1 to 5 μm^2/s. As the recovery of fluorescent molecules is intrinsically tied to the diffusion constant, the recovery time was adapted in respect of the value of D. The particular values of t_{rec} were predetermined by separate simulations such that the number of resolvable particles in the analysis image (data rate) is roughly kept constant for each value of D.

The results presented in Fig. 20 show that incomplete bleaching affects more molecules in case of increased mobility. The total number of particles, entering and leaving the illuminated area during photobleaching, increases and accordingly the number of incompletely bleached molecules. For simulations of particles with $D > 3$ μm^2/s, the exact photobleaching probability within the edge zone seems to be of minor importance as the differences in the apparent dimer fraction between the uniform and the diffracted laser profile are vanishing.

5.2.5 Influence of aperture size on incomplete photobleaching

In order to examine the effects of a larger aperture size on the detection of incompletely bleached molecules, the following simulations were carried out. A homogeneous population of 100 % dimers at $\rho_{surface} = 100$ dimers/μm^2 and $D = 0.5$ μm^2/s was simulated with a varying side length of a squared aperture between 3 and 15 μm. Since the photobleached area was varied in size, the recovery time was predetermined in separate simulations as before and adapted accordingly, providing a roughly constant data rate. The total number of incompletely bleached molecules increases linearly with the aperture size as illustrated in Fig. 21B. This originates from the enlarged edge region where incomplete photobleaching takes place due to diffusion and diffraction effects. On the other hand, by increasing the area and the recovery time, a larger number of molecules will be able to diffuse into the bleached region from more distant locations than for shorter recovery times and smaller apertures. This leads to the previously discussed dilution of partially bleached molecules. A priori it is thus unknown whether a large aperture size could improve the performance of the experiment.

The increase in dimer fraction in Fig. 21A shows a reduced detection of partially bleached

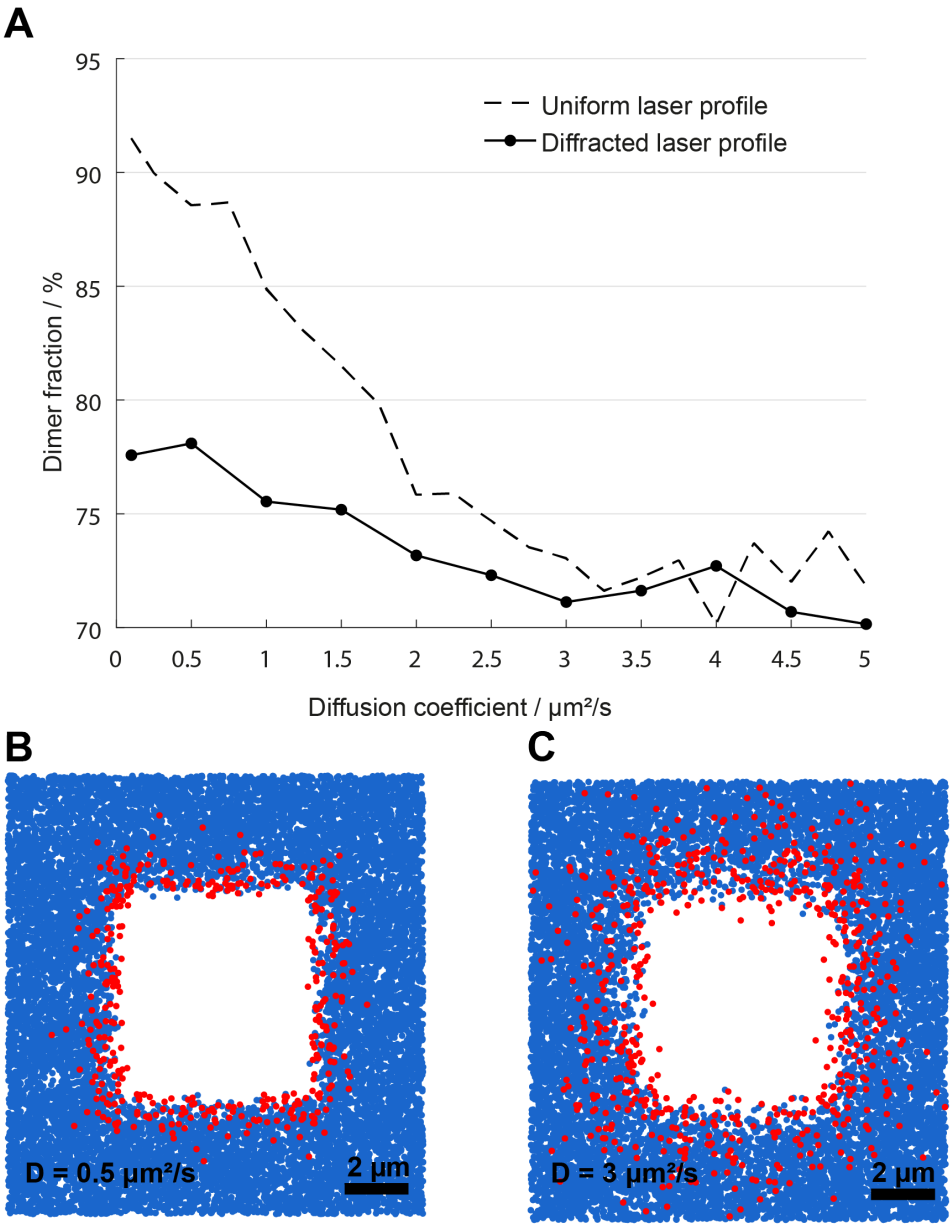

Figure 20: **A** Resulting dimer fraction (original fraction: 100 %) for varying diffusion coefficient in a simulated TOCCSL experiment. **B-C** Simulated post-bleach situation for an initially fully fluorescent dimer population (blue). The edge zone containing incompletely bleached dimers (red) is shown for a diffusion coefficient $D = 0.5\ \mu\text{m}^2/\text{s}$ (panel B) and $D = 3\ \mu\text{m}^2/\text{s}$ (panel C). For the latter case, the effects of incomplete bleaching are more pronounced due to increased mobility.

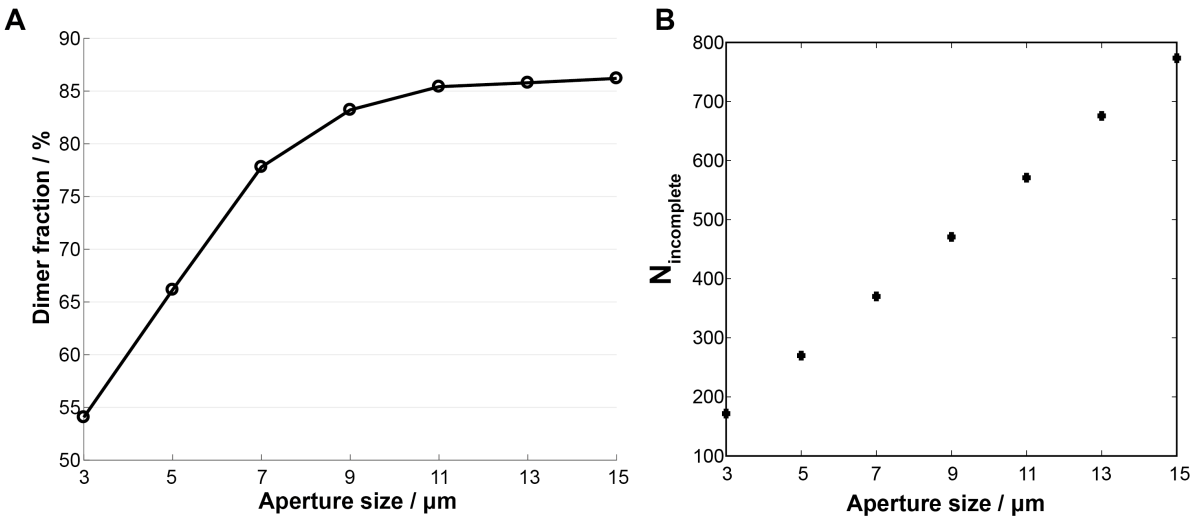

Figure 21: Incomplete photobleaching for varying aperture sizes in a TOCCSL experiment. Simulations were done for $t_{bleach} = 500$ ms, $D = 0.5$ μm^2/s and $\rho = 100$ dimers/μm^2. The size of the squared aperture and accordingly the recovery time were varied. **A** Resulting dimer fraction as a function of aperture size. **B** Average total number of partially bleached dimers per run as a function of aperture size.

molecules for large aperture sizes, although the curve flattens for larger apertures. It indicates that the dilution of concentration of incompletely bleached particles toward the center is dominating. However, it is increasingly compensated by the rising absolute number of incompletely bleached particles. In any case, a large aperture results in pronounced depletion of fluorescence. The number of conductible experiments per cell is reduced. Thus, the experimental effort increases in order to obtain the same amount of data as with a small aperture. The distribution of the increased number of partially bleached clusters over the course of multiple measurements on the same cell has to be considered as well.

5.3 Mobility differences

A TOCCSL experiment with a mixed population of two molecule species A and B with distinct values for the diffusion coefficient $D_A > D_B$ shall be assumed. After recovery, molecule B is less likely to be found in the analyzed region than molecule A due to reduced mobility. The quantification of this effect was done via simulations with an equally distributed population of two species A and B. The diffusion constant of the first species D_A was kept constant at $D_A = 0.5\frac{\mu m^2}{s}$, whereas the diffusion constant of the second species D_B was calculated according to $D_B = D_A \cdot R$, where R thus represents the ratio $\frac{D_B}{D_A}$, which was varied between 0.2 and 1. The surface density $\rho_{surface} = 100$ dimers/μm^2, the recovery time $t_{rec} = 1.5$ s and the photobleaching

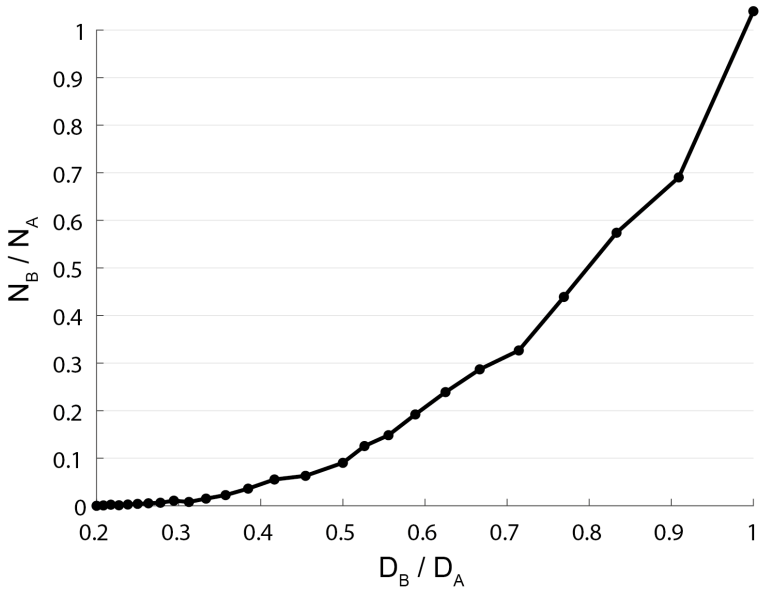

Figure 22: Ratio of detected particles for a simulated TOCCSL experiment with two distinct molecule species A and B with $D_A \geq D_B$. Due to decreased mobility of species B, less particles of B are detected.

time $t_{bleach} = 500$ ms were kept constant. In order to illustrate the isolated impact caused by mobility differences, ideal photobleaching was simulated, meaning an instantaneous and complete photobleaching of all fluorophores inside the aperture.

The results, illustrated in Fig. 22, exhibit in fact significant impacts on the detected fractions. For $D_A = D_B$, or $R = 1$, the simulated fractions of the two species A and B are around 50 %. Statistical fluctuations lead to small deviations. As the diffusion coefficient of species B is reduced, the determined relative fraction decreases significantly. In case of $R = 0.2$, where D_B is only 20 % of D_A, almost no particles of the slower diffusing species B are detectable, leading to a detected fraction of approximately 100 % for species A. Since incomplete bleaching was not taken into account for these simulations, the results were found to be independent of the absolute values of D_A and D_B. The results are therefore in agreement with analytically calculated results by *Ruprecht et al.* in [35].

5.4 False colocalizations

As described in Sec. 3.4, a TOCCSL experiment holds the possibility of detecting random encounters of two distinct molecules as a single diffraction limited signal. To investigate the detection of false positives, simulations were done with 100 % monomers. This allows for direct

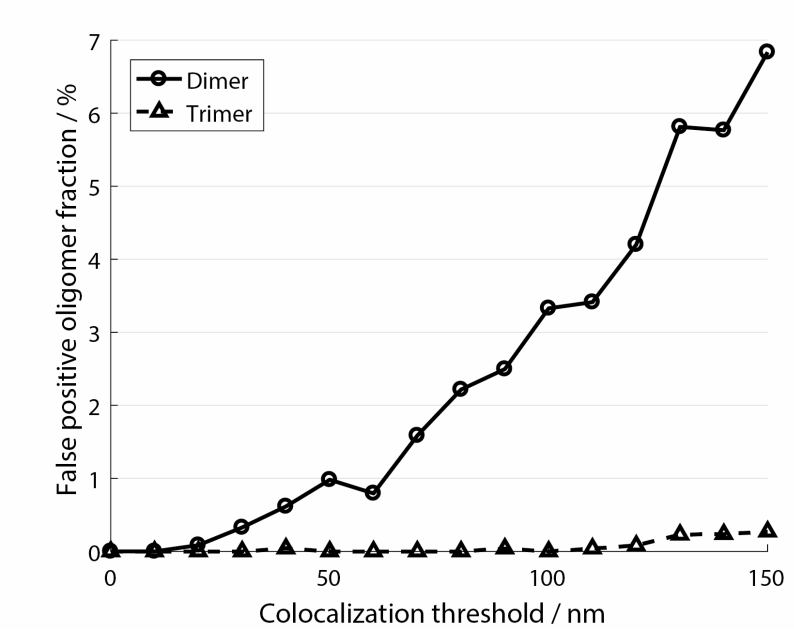

Figure 23: Fraction of detected false positives for a 100 % monomeric fraction in a simulated TOCCSL experiment. The oligomeric fractions result from random encounters of monomeric particles and are shown as function of the colocalization threshold.

identification of the falsely detected oligomers because all higher-order oligomeric fractions result solely from random encounters. Basic parameters were chosen as $t_{bleach} = 500$ ms, $\rho_{surface} = 100$ particles/μm^2, $t_{rec} = 1.5$ s and $D = 0.5$ μm^2/s. The colocalization threshold d_{FP} (see Sec. 4.6.1) was varied from 0 to 150 nm. Since only monomers were simulated, no incomplete photobleaching is involved.

The results shown in Fig. 23 indicate minor effects with a maximum of less than 7 % detected dimers and less than 1 % trimers in the case of a the maximum simulated distance threshold of 150 nm. If the available data analysis tools do not allow for discrimination of two signals separated by a distance of more than 150 nm, the detection of false positives becomes more pronounced and should be considered accordingly. Fig. 23 is qualitatively in agreement with analytical calculations done by *Ruprecht et al.* in [35]. There, the fraction of false colocalizations for two distinct species A and B are calculated. Therefore, the results are not directly comparable.

5.4.1 Influence of aperture size on false colocalizations

A strategy that comes into consideration to reduce the detection of false colocalizations, is the increase in aperture size. A larger area of the cell surface is thereby photobleached. By proper

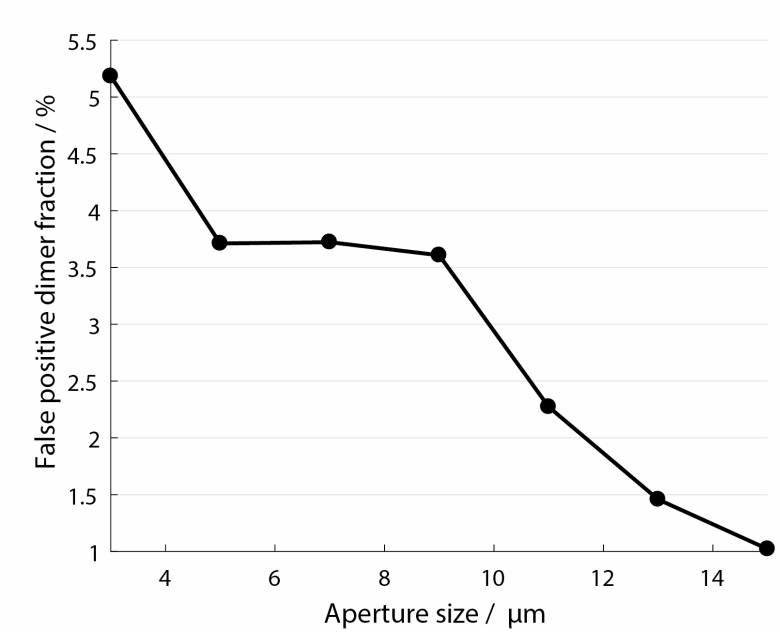

Figure 24: Simulated detected oligomer fractions in TOCCSL experiments with varying aperture sizes. The colocalization threshold was kept constant at 100 nm. The original fraction was assumed to be 100 % monomers. The resulting dimer detection solely comes from false-positive detection of random colocalizations. Detection of oligomers of higher degree is negligible.

choice of recovery time, the surface density in the analyzed ROI and hence the probability of random encounters of two particles is reduced. The simulations were performed using the same basic parameters as described in Sec. 5.2.5 except that a population of 100 % monomers instead of dimers was simulated to emphasize the effect of false colocalizations. These were taken into account with a constant distance threshold $d_{FP} = 100$ nm. Fig. 24 shows a decrease in oligomeric fractions with increasing aperture size. Hence, increasing the aperture size is an effective measure for reducing the detection of false positives due to a decrease in surface density within the analyzed region.

5.5 Combination of error sources

The simulations discussed in the previous sections, deal with the isolated influence of a single error source. In a TOCCSL experiment, some of them will be more pronounced than others. Some error sources even counteract other errors, leading to a complex interaction of all different influences. The individual influences on the experimental outcome always depend on the particular set of parameters. For an exemplary parameter set, the following simulations aim to illustrate the combined influences of the given error sources: incomplete photobleaching, mo-

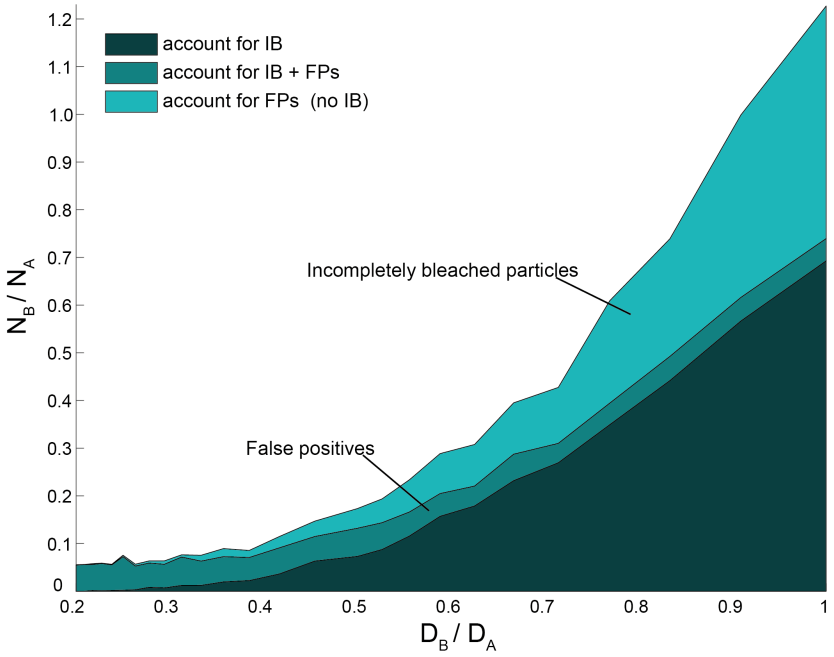

Figure 25: Combination of error sources for simulated TOCCSL experiments with 50 % monomers and 50 % dimers. The ratio of detected particles N_2/N_1 is shown for different ratios of diffusion coefficients D_2/D_1. The influence of differences between D_1 and D_2 on the result is predominant. Incomplete bleaching (IB) further reduces the detected number of dimers. In turn, the detection of false positives (FPs) increases the dimer fraction.

bility differences (depending on the number of subunits) and false positive detection of random colocalizations. The simulations were done for a 50:50-distribution of dimers and monomers with distinct diffusion coefficients D_1 and D_2, respectively. As in Sec. 5.3, the diffusion coefficient of the first species (in this case the monomeric fraction) is kept constant at $D_1 = 0.5\ \mu\text{m}^2/\text{s}$ while varying the ratio of diffusion coefficients D_2/D_1 between 0.2 and 1. In addition, incomplete bleaching and the detection of false positives with a colocalization threshold of $d_{FP} = 100$ nm is taken into account.

The ratio of detected particles N_2/N_1 is shown in Fig. 25 as a function of the ratio of diffusion coefficients. The number of detected particles N_2 decreases with decreasing D_2. Incomplete photobleaching further reduces the number of detected dimers, whereas the detection of false colocalizations leads to a small increase in the fraction and, hence, in the ratio N_2/N_1. The account for false positives results in a ratio $N_2/N_1 \approx 1.2$ compared to $N_2/N_1 = 1$, which would be expected without false positives. The counteracting influences of incomplete photobleaching and detection of false positives are given by the respective areas below the curves. The effect of

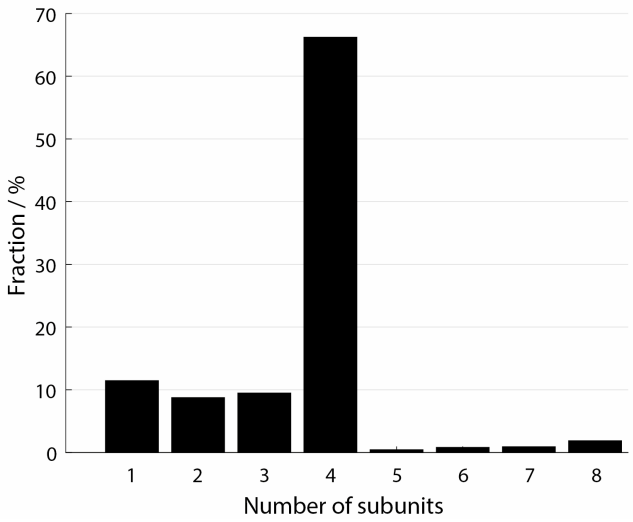

Figure 26: TOCCSL simulation for a pure tetrameric population. A diffusion coefficient of 0.5 μm^2/s, a recovery time $t_{rec} = 1.5$ s and a surface density of 100 tetramers/μm^2 were assumed as parameters.

underrepresentation in the analyzed region due to reduced mobility, however, is predominant. Although the ratio N_2/N_1 is not affected by the absolute values of D_1 and D_2, the extent of incomplete photobleaching is strongly dependent on these values (see Sec. 5.2.4).

5.6 Simulation of a tetrameric population

Since some biomolecules in nature appear as a tetramer, a simulation was performed with a pure tetrameric population and a fixed parameter set of typical experimental values. The resulting apparent oligomeric distribution is shown in Fig. 26. Incomplete bleaching could lead to a detection of less than 70 % tetramers and around 10 % monomers, dimers and trimers each. A few percent in higher order oligomeric fractions up to octamers result from random colocalizations of a combination of tetramers and lower order oligomers. False positives do not contribute significantly to the lower oligomeric fractions due to the relatively low fractions of partially bleached oligomers. They are therefore not explicitly shown in Fig. 26.

6 Discussion

6.1 Photobleaching

The approximated laser intensity profile used for the TOCCSL simulations was not intended to be an exact representation of the real laser profile but a simple approximation in order to estimate the influence of diffraction on the photobleaching probability. Gaussian functions are chosen as a simple way to approximate the edges of the measured laser profile compared to a complex solution of the diffraction integral for a slit. The measurements in order to characterize the laser profile was done by exciting a homogeneous sample of monomeric GFP molecules in the plasma membrane of live CHO cells at a laser intensity of $\sim$5 kW/cm^2. The laser intensity in the xy-plane was assumed to be directly proportional to the fluorescence signal of the GFP molecules. This is - in approximation - justified because the laser intensity for excitation of the fluorophores is far from the saturation intensity (see Fig. 27).

Regarding photobleaching, many different models for photobleaching mechanisms of fluorophores and their quantification have been suggested. For this work, a two-component exponential function was used to approximate the experimental bleaching curve of GPI-mGFP (Sec. 4.4). The fit function is simply a good approximation (see Fig. 12) and was chosen to describe the curve analytically without assumption of a particular underlying model.

For the simulation of the photobleaching process, an equal bleaching probability for the individual fluorophores of the same aggregate was assumed irrespective of the number of subunits or colocalized fluorophores. It is possible, however, that the proximity of other (fluorescent) molecules affects the fluorescent behavior of the individual fluorophores (quenching), e.g due to electromagnetic interaction. Under which circumstances these interactions occur and how they influence the fluorescent characteristics would be subject to further studies. In [63], for example, interactions of Rhodamin 6G molecules with a two-dimensional array of silver nanoparticles were observed. There, the overall fluorescence intensity as well as the photobleaching probability was increased.

Between two close fluorophores, Förster resonance energy transfer (FRET) or Dexter electron transfer are possible quenching mechanisms. FRET is typically occurring at distances up to 10 nm due to dipole-dipole interactions between an excited donor and an acceptor molecule. At even smaller distances, the overlap of molecular orbitals of two fluorophores can lead to a Dexter

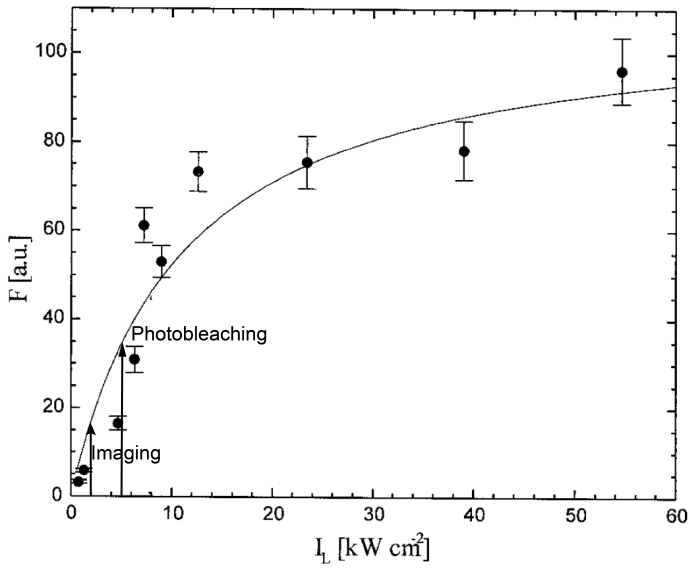

Figure 27: Fluorescence saturation curve of GFP molecules in solution. The fluorescence signal F reaches a plateau for high laser intensities I_L. Photobleaching is performed at $I_L \sim 5$ kW/cm^2, imaging at $I_L < 2$ kW/cm^2. Figure adapted from [62].

electron transfer. In case of two molecules of the same type (homo-FRET), however, these two mechanisms do not change the fluorescent intensity of the signal (but the polarization).
Moreover, fluorophores could exhibit blinking behavior, i.e. switching between active and inactive states of fluorescence. To a certain extent, blinking of fluorophores could alter the results of a TOOCSL experiment. It could lead to an increase in detection of lower order oligomer fractions due to the possibility that some fluorophores are in an inactive state during image recording after recovery. If that happens for individual fluorophores that are part of an aggregate, it will be detected as an oligomer with less subunits. This would assume a blinking behavior on a time scale exceeding the illumination time for imaging. Blinking during the bleaching pulse, however, could prevent photobleaching of individual fluorophores. Thus, the results could also be influenced by incomplete bleaching of blinking fluorophores. In this work, however, blinking statistics have not been taken into account since it is not assumed to be a major issue and is mostly preventable by proper choice of fluorophores.

In live cell experiments, occasionally the edge of the cell surface that is attached to the slide, is part of the illuminated area. This is often inevitable due to the shape or size of the cell, especially when studying elongate cells. In this case, one dimension of the illuminated area of the cell is confined by the aperture and the other dimension by the cell itself. Thus, the photobleaching laser pulse is targeting the edge of the attached plasma membrane. Then, the

penetration depth of the evanescent field is not negligible. Near the edge, it reaches parts of the plasma membrane, which are not attached to the glass surface. The typical penetration depth is around 100 nm. With increasing distance from the glass slide, the laser intensity is reduced leading to incomplete photobleaching of molecules.

6.2 Multiple runs on a single cell

When conducting a live cell TOCCSL experiment, usually multiple measurements are taken on the same cell. This can be done until the majority of fluorescent molecules is photobleached and the surface density is too low to employ reasonable measurements. Depletion of fluorescence occurs during the individual measurement runs - on the one hand by intentional photobleaching at high laser intensity and on the other hand by unintended photobleaching during imaging at low laser intensity. The effect of incomplete bleaching during the photobleaching time t_{bleach} is extensively discussed in this work, whereas the bleaching during imaging has not been subject so far. This is due to the fact that the individual simulation runs were performed assuming a "new cell" at a constant initial surface density. Multiple runs on the same cell, however, could be accompanied by an increased detection of partially bleached particles. For a single run on a "new cell", only the particles that have been bleached in this particular run have to be taken into account.

The imaging laser intensity is typically significantly lower than the intensity for intentional photobleaching. Hence, the probability for incomplete photobleaching of clusters is greater than for a high intensity laser pulse. During repeated measurements on the same cell, partially bleached particles are able to spread all over the plasma membrane due to Brownian motion. This could lead to the reappearance of particles which have been partially bleached in a former run. These molecules could therefore contribute to the results by diffusing in the analyzed area during the recovery time. The consequences have not yet been quantified but could, in principle, be investigated by adjusting the simulations.

On the other hand, repeated runs on the same cells can be used to investigate the stability of oligomers. Due to dissociation and recombination of both bleached and non-bleached subunits, the experimentally determined oligomeric distribution is shifted towards smaller structures for an increasing number of runs on the same cell. Stable oligomers do not alter the oligomeric distribution over the course of an experiment with repeated runs. This has been used by *Anderluh*

et al. in [39] to show the rapid exchange of subunits between oligomers of the human serotonin transporter (hSERT) in the endoplasmatic reticulum (ER) and PIP_2-mediated stabilization of the SERT oligomers in the plasma membrane. For stable oligomers, the results over the course of multiple measurements on the same cell did not change significantly. Hence, the increase in impact of incompletely bleached particles with an increasing number of measurement runs is not assumed to be a major problem. However, the influence is again dependent on the particular experimental parameters and therefore should not be generalized.

6.3 Measurement strategies and optimization of TOCCSL experiments

If the photobleaching behavior and other basic parameters (diffusion coefficient, surface density, etc.) are known, errors could, in principle, be compensated by carrying out simulations with the respective parameter set. The correct oligomeric fractions could be obtained by varying the initial distribution of oligomers and comparing the computational outcome to the experimental results. A simulation, however, is not a perfect reproduction of an experiment and it is, in any case, recommended to optimize the experimental parameters. This can be done according to the simulation results that have been discussed in this work and revealed several fundamental dependencies between error sources and experimental parameters. The most important findings are summarized in the following.

Recovery time

Concerning the effects of incomplete photobleaching, simulations revealed that it is beneficial to extend the recovery time as much as possible. Incompletely bleached clusters will be diluted to a maximal degree, which results in more accurate measurements. On the other hand, it is quite evident that the number of false colocalizations is increasing with the recovery time. The resulting high surface density increases the probability of two particles to be located within a small radius. The impact of incomplete bleaching, however, usually dominates the results, which is why a longer recovery time is beneficial. Furthermore, it is more convenient to correct for false colocalizations than for incomplete bleaching since analytic solutions are available [35]. For mixed populations with distinct values of D, deviations in the number of detected particles due to reduced mobility would also be more pronounced. This effect could, however, be compensated by data post-processing as well, if the diffusion coefficients are known or could be determined

experimentally. The drawback of a long recovery time and the resulting high surface density in the analyzed region, is a low number of resolvable particles.

Photobleaching time

As shown in Fig. 17, after a certain bleaching time, further photobleaching does not have an effect on the results. Although it is important to apply an illumination pulse for at least a minimal amount of time in order to completely bleach the particles in the central region of the ROI, further bleaching would only lead to an increase of incompletely bleached aggregates. Hence, it is suggested that the bleaching time is chosen as long as necessary to bleach the central region sufficiently but as short as possible in order to avoid further incomplete bleaching. This is especially of importance, if repeated measurements on the same cell are conducted.

Aperture size

In the present work, the influence of the aperture size defining the size of the photobleached area, was studied in two different contexts. First, an increase in aperture size is an effective measure to decrease the number of detected false colocalizations since surface density in the analysis region is drastically reduced. Second, a larger aperture size could also reduce the detection of incompletely bleached oligomers. On the other hand, the increase in the absolute number of incompletely bleached molecules is counteracting this effect. Thus, if the aperture size is already increased to a certain degree, further enlargement will show only minor beneficial effects.

In general, when the aperture size is increased, the choice of a sufficiently long recovery time should be considered. The error resulting from a recovery time being too short, could be predominant and overlay the benefit of an enlarged aperture. Apart from beneficial effects, a larger aperture size increases depletion and reduces the number of possible measurements per cell.

Mobility differences

In order to overcome the impact of mobility differences between distinct species or oligomeric fractions, it is necessary to quantify their diffusive behavior. Given the knowledge of diffusion coefficients, it is possible to compensate differences in mobility by data post-processing. With a TOCCSL setup, the diffusion coefficients of the target molecules can routinely be determined

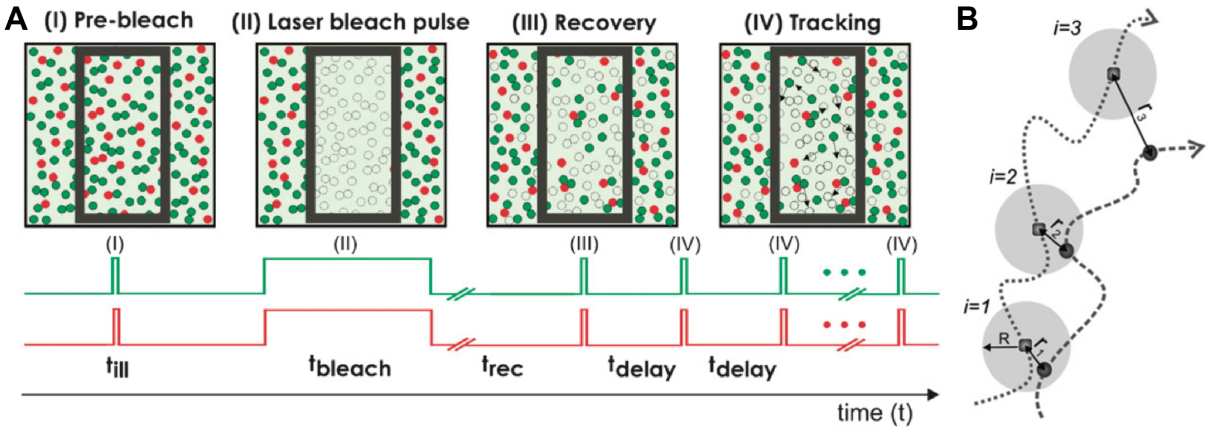

Figure 28: **A** Schematic and illumination timing protocol for a two-color TOCCSL experiment. **B** Tracking of colocalized signals for exclusion of false positives. The probability for randomly colocalized particles to stay associated is rapidly decreasing with the number of acquired trajectory steps. Figures adapted from [35].

by single molecule tracking experiments. It can either be done in separate experiments or included in the TOCCSL illumination protocol by recording a series of consecutive images with a predefined time lag during recovery. This is illustrated in Fig. 28 for a two-color experiment. After analyzing the trajectories and determination of the diffusion coefficients, the obtained fractions could be recalculated based on the results of stochastic simulations with the respective parameter set or on analytic calculations as done in [35].

Tracking of colocalized particles

As a strategy to rule out random encounters, tracking of colocalized events could reduce the detection of false positives. It could be employed in addition to or instead of an enlargement of the aperture, which a priori reduces the probability for detecting false positives. Accidental colocalization events show no correlated movement and will thus separate over time as shown in Fig. 28.

Laser profile

For photobleaching and imaging in a TOCCSL experiment (and in general for fluorescence microscopy), a homogeneous laser intensity across the field of view is important. A typical laser intensity profile is represented by a Gaussian beam profile (TEM_{00} mode). However, after appropriate expansion of the laser beam, the approximately homogeneous inner beam region can be used for measurements. Another possibility is homogenization of the laser beam. A recently developed microlens array-based illumination system is presented in [64]. Flat illumination for

field-independent imaging (FIFI) enabled a homogeneously illuminated field of view of 100x100 μm^2. As to avoid far-field diffraction effects, which would lead to oscillating patterns in the laser intensity profile (Eq. 15), it is essential that the width of the aperture is large compared to the wavelength of the laser.

Multiple runs on the same cell

For repeated measurements on the same cell, it is suggested to reduce the number of runs per cell to a minimum level in order to avoid the impact of reappearing partially bleached aggregates during consecutive measurements. An illumination timing protocol with variable recovery times depending on the advance of measurements in a cell is preferable since the surface density of the fluorescent molecules is constantly depleted by illumination. In certain cases, however, it is inevitable to conduct multiple runs on the same cells, e.g. for investigation of oligomerization dynamics or cell-to-cell variabilities.

References

[1] Bruce Alberts. *Molecular biology of the cell*. Garland science, 2017.

[2] S. J. Singer and Garth L. Nicolson. "The Fluid Mosaic Model of the Structure of Cell Membranes". In: *Science* 175.4023 (1972), pp. 720–731.

[3] D. M. Engelman. "Membranes are more mosaic than fluid". In: *Nature* 438.7068 (2005), pp. 578–80.

[4] E. Sevcsik and G. J. Schutz. "With or without rafts? Alternative views on cell membranes". In: *Bioessays* 38.2 (2015), pp. 129–39.

[5] Akihiro Kusumi et al. "Paradigm shift of the plasma membrane concept from the two-dimensional continuum fluid to the partitioned fluid: high-speed single-molecule tracking of membrane molecules". In: *Annu. Rev. Biophys. Biomol. Struct.* 34 (2005), pp. 351–378.

[6] Michael J Saxton and Ken Jacobson. "Single-particle tracking: applications to membrane dynamics". In: *Annual review of biophysics and biomolecular structure* 26.1 (1997), pp. 373–399.

[7] Jean-Luc Popot and Donald M Engelman. "Membrane protein folding and oligomerization: the two-stage model". In: *Biochemistry* 29.17 (1990), pp. 4031–4037.

[8] Donald M. Engelman et al. "Membrane protein folding: beyond the two stage model". In: *FEBS Letters* 555.1 (2003), pp. 122–125.

[9] Axel Ullrich and Joseph Schlessinger. "Signal transduction by receptors with tyrosine kinase activity". In: *Cell* 61.2 (1990), pp. 203–212.

[10] David S Goodsell and Arthur J Olson. "Structural symmetry and protein function". In: *Annual review of biophysics and biomolecular structure* 29 (2000).

[11] Monika Suchanek, Anna Radzikowska, and Christoph Thiele. "Photo-leucine and photo-methionine allow identification of protein-protein interactions in living cells". In: *Nature methods* 2.4 (2005), p. 261.

[12] Norihiro Kotani et al. "Biochemical visualization of cell surface molecular clustering in living cells". In: *Proceedings of the National Academy of Sciences* 105.21 (2008), pp. 7405–7409.

[13] Igor Stagljar and Stanley Fields. "Analysis of membrane protein interactions using yeast-based technologies". In: *Trends in biochemical sciences* 27.11 (2002), pp. 559–563.

[14] Michelle A Digman et al. "Mapping the number of molecules and brightness in the laser scanning microscope". In: *Biophysical journal* 94.6 (2008), pp. 2320–2332.

[15] Peter Nagy et al. "Distribution of resting and ligand-bound ErbB1 and ErbB2 receptor tyrosine kinases in living cells using number and brightness analysis". In: *Proceedings of the National Academy of Sciences* 107.38 (2010), pp. 16524–16529.

[16] Petra Schwille, Franz-Josef Meyer-Almes, and Rudolf Rigler. "Dual-color fluorescence cross-correlation spectroscopy for multicomponent diffusional analysis in solution". In: *Biophysical journal* 72.4 (1997), pp. 1878–1886.

[17] Kirsten Bacia, Sally A Kim, and Petra Schwille. "Fluorescence cross-correlation spectroscopy in living cells". In: *Nature methods* 3.2 (2006), p. 83.

[18] Mario Brameshuber and Gerhard J Schütz. "How the sum of its parts gets greater than the whole". In: *Nature methods* 5.2 (2008), pp. 133–134.

[19] Shalini T Low-Nam et al. "ErbB1 dimerization is promoted by domain co-confinement and stabilized by ligand binding". In: *Nature structural molecular biology* 18.11 (2011), pp. 1244–1249.

[20] Sarah L Latty et al. "Referenced single-molecule measurements differentiate between GPCR oligomerization states". In: *Biophysical journal* 109.9 (2015), pp. 1798–1806.

[21] Maximilian H Ulbrich and Ehud Y Isacoff. "Subunit counting in membrane-bound proteins". In: *Nature methods* 4.4 (2007), p. 319.

[22] Richard Hallworth and Michael G Nichols. "The single molecule imaging approach to membrane protein stoichiometry". In: *Microscopy and Microanalysis* 18.4 (2012), pp. 771–780.

[23] Eric Betzig et al. "Imaging intracellular fluorescent proteins at nanometer resolution". In: *Science* 313.5793 (2006), pp. 1642–1645.

[24] Samuel T Hess, Thanu PK Girirajan, and Michael D Mason. "Ultra-high resolution imaging by fluorescence photoactivation localization microscopy". In: *Biophysical journal* 91.11 (2006), pp. 4258–4272.

[25] Michael J Rust, Mark Bates, and Xiaowei Zhuang. “Sub-diffraction-limit imaging by stochastic optical reconstruction microscopy (STORM)”. In: *Nature methods* 3.10 (2006), pp. 793–795.
[26] Mike Heilemann et al. “Subdiffractionâresolution fluorescence imaging with conventional fluorescent probes”. In: *Angewandte Chemie International Edition* 47.33 (2008), pp. 6172–6176.
[27] Robert PJ Nieuwenhuizen et al. “Quantitative localization microscopy: effects of photophysics and labeling stoichiometry”. In: *PloS one* 10.5 (2015), e0127989.
[28] Franziska Fricke et al. “One, two or three? Probing the stoichiometry of membrane proteins by single-molecule localization microscopy”. In: *Scientific reports* 5 (2015).
[29] Florian Baumgart et al. “Varying label density allows artifact-free analysis of membrane-protein nanoclusters”. In: *Nature methods* 13.8 (2016), pp. 661–664.
[30] Ulrike Schnell et al. “Immunolabeling artifacts and the need for live-cell imaging”. In: *Nature methods* 9.2 (2012), pp. 152–158.
[31] Donna R Whelan and Toby DM Bell. “Image artifacts in single molecule localization microscopy: why optimization of sample preparation protocols matters”. In: *Scientific reports* 5 (2015).
[32] Kenji AK Tanaka et al. “Membrane molecules mobile even after chemical fixation”. In: *Nature Methods* 7.11 (2010), pp. 865–866.
[33] Manuel Moertelmaier et al. “Thinning out clusters while conserving stoichiometry of labeling”. In: *Applied Physics Letters* 87.26 (2005), p. 263903.
[34] M. Brameshuber et al. “Imaging of mobile long-lived nanoplatforms in the live cell plasma membrane”. In: *J Biol Chem* 285.53 (2010), pp. 41765–71.
[35] Verena Ruprecht, Mario Brameshuber, and Gerhard J. Schütz. “Two-color single molecule tracking combined with photobleaching for the detection of rare molecular interactions in fluid biomembranes”. In: *Soft Matter* 6.3 (2010), pp. 568–581.
[36] Josef Madl et al. “Resting state Orai1 diffuses as homotetramer in the plasma membrane of live mammalian cells”. In: *Journal of Biological Chemistry* 285.52 (2010), pp. 41135–41142.
[37] Andreas Anderluh et al. “Single molecule analysis reveals coexistence of stable serotonin transporter monomers and oligomers in the live cell plasma membrane”. In: *Journal of Biological Chemistry* 289.7 (2014), pp. 4387–4394.
[38] Mario Brameshuber et al. “Oxidized phospholipids inhibit the formation of cholesterol-dependent plasma membrane nanoplatforms”. In: *Biophysical journal* 110.1 (2016), pp. 205–213.
[39] Andreas Anderluh et al. “Direct PIP2 binding mediates stable oligomer formation of the serotonin transporter”. In: *Nature communications* 8 (2017), p. 14089.
[40] Vladislav Belyy et al. “PhotoGate microscopy to track single molecules in crowded environments”. In: *Nature communications* 8 (2017).
[41] Makio Tokunaga, Naoko Imamoto, and Kumiko Sakata-Sogawa. “Highly inclined thin illumination enables clear single-molecule imaging in cells”. In: *Nature methods* 5.2 (2008), p. 159.
[42] Loling Song et al. “Photobleaching kinetics of fluorescein in quantitative fluorescence microscopy”. In: *Biophysical journal* 68.6 (1995), pp. 2588–2600.
[43] Erwin Füreder-Kitzmüller et al. “Non-exponential bleaching of single bioconjugated Cy5 molecules”. In: *Chemical Physics Letters* 404.1-3 (2005), pp. 13–18.
[44] Sarah A Mutch et al. “Deconvolving single-molecule intensity distributions for quantitative microscopy measurements”. In: *Biophysical journal* 92.8 (2007), pp. 2926–2943.
[45] D Axelrod, T P Burghardt, and N L Thompson. “Total Internal Reflection Fluorescence”. In: *Annual Review of Biophysics and Bioengineering* 13.1 (1984), pp. 247–268.
[46] Daniel Axelrod. “Cell-substrate contacts illuminated by total internal reflection fluorescence”. In: *The Journal of cell biology* 89.1 (1981), pp. 141–145.
[47] M. Brameshuber and G. J. Schütz. “Single Molecule Measurements in Membranes”. In: *Comprehensive Biophysics* 5 (2012), pp. 337–365.
[48] Russell E Thompson, Daniel R Larson, and Watt W Webb. “Precise nanometer localization analysis for individual fluorescent probes”. In: *Biophysical journal* 82.5 (2002), pp. 2775–2783.
[49] Kim I Mortensen et al. “Optimized localization analysis for single-molecule tracking and super-resolution microscopy”. In: *Nature methods* 7.5 (2010), pp. 377–381.

[50] Douglas B Murphy. *Fundamentals of light microscopy and electronic imaging*. Vol. 1. John Wiley Sons, 2001.
[51] Emil Wolf Max Born. *Principles of Optics*. 7th ed. Cambridge University Press.
[52] Junghae Suh, Michelle Dawson, and Justin Hanes. "Real-time multiple-particle tracking: applications to drug and gene delivery". In: *Advanced drug delivery reviews* 57.1 (2005), pp. 63–78.
[53] Valeria Levi and Enrico Gratton. "Exploring dynamics in living cells by tracking single particles". In: *Cell biochemistry and biophysics* 48.1 (2007), p. 1.
[54] John C Crocker and David G Grier. "Methods of digital video microscopy for colloidal studies". In: *Journal of colloid and interface science* 179.1 (1996), pp. 298–310.
[55] PG Saffman and M Delbrück. "Brownian motion in biological membranes". In: *Proceedings of the National Academy of Sciences* 72.8 (1975), pp. 3111–3113.
[56] BD Hughes, BA Pailthorpe, and LR White. "The translational and rotational drag on a cylinder moving in a membrane". In: *Journal of Fluid Mechanics* 110 (1981), pp. 349–372.
[57] Ali Naji, Alex J Levine, and Philip A Pincus. "Corrections to the Saffman-Delbrück mobility for membrane bound proteins". In: *Biophysical journal* 93.11 (2007), pp. L49–L51.
[58] Y Gambin et al. "Lateral mobility of proteins in liquid membranes revisited". In: *Proceedings of the National Academy of Sciences of the United States of America* 103.7 (2006), pp. 2098–2102.
[59] Pietro Cicuta, Sarah L Keller, and Sarah L Veatch. "Diffusion of liquid domains in lipid bilayer membranes". In: *The journal of physical chemistry B* 111.13 (2007), pp. 3328–3331.
[60] V Prasad, SA Koehler, and Eric R Weeks. "Two-particle microrheology of quasi-2D viscous systems". In: *Physical review letters* 97.17 (2006), p. 176001.
[61] Imre Gombos et al. "Membrane-lipid therapy in operation: the HSP co-inducer BGP-15 activates stress signal transduction pathways by remodeling plasma membrane rafts". In: *PLoS One* 6.12 (2011), e28818.
[62] Ulrich Kubitscheck et al. "Imaging and tracking of single GFP molecules in solution". In: *Biophysical Journal* 78.4 (2000), pp. 2170–2179.
[63] H Ditlbacher et al. "Electromagnetic interaction of fluorophores with designed two-dimensional silver nanoparticle arrays". In: *Applied Physics B: Lasers and Optics* 73.4 (2001), pp. 373–377.
[64] Kyle M Douglass et al. "Super-resolution imaging of multiple cells by optimised flat-field epi-illumination". In: *Nature photonics* 10.11 (2016), p. 705.

A Input parameters for TOCCSL simulations

The following parameters were used for the simulations discussed in the results section.

Variable	*Convergence*	*Bleaching time*	*Recovery time*
n_nmer	2	2	2
$fraction$	[0 1]	[0 1]	[0 1]
D	0	0	0
$D(2)$	0.5	0.5	0.5
$aperture\_size\_x$	7	7	7
$aperture\_size\_y$	7	7	7
$density$	250	100	100
t_bleach	500	0 : 25 : 700	500
t_rec	1.5	1.5	var
$stepno\_second$	0 : 25 : 500	300	300
$laser\_shape$	$'uniform'$	$'diffraction' + 'uniform'$	$diffraction' + 'uniform'$
res_limit	0.3	0.3	0.3
fp_limit	0	0	0
$innermost$	*all particles*	15	15
$gridsize$	21	21	21

Variable	$Diffusion\ coeffiecient$	$Aperture\ size - IB$
n_nmer	2	2
$fraction$	[0 1]	[0 1]
D	0	0
$D(2)$	0.1 : 0.5 : 5	0.5
$aperture\_size\_x$	7	[3 : 2 : 15]
$aperture\_size\_y$	7	[3 : 2 : 15]
$density$	100	100
t_bleach	500	500
t_rec	[4.5 1.85 0.98 0.68 0.51 0.43 ...	[0.3 0.55 1.92 3.4 4 4.5 5]
	... 0.36 0.31 0.28 0.24 0.22]	
$stepno\_second$	300	300
$laser\_shape$	$'diffraction' + 'uniform'$	$'diffraction'$
res_limit	0.3	0.3
fp_limit	0	0.15
$innermost$	15	15
$gridsize$	28	35

Variable	*Mobility differences*	*False Positives*	*Aperture size – FP*
n_nmer	2	1	1
fraction	[0.5 0.5]	1	1
D	0.5	0.5	0.5
$D(2)$	$D(2) = D(1)/R$	–	–
	$R = 1 : 0.1 : 2$ *and* $2.2 : 0.2 : 5$		
aperture_size_x	7	7	$[3 : 2 : 15]$
aperture_size_y	7	7	$[3 : 2 : 15]$
density	100	100	100
t_bleach	500	500	500
t_rec	1.5	1.5	[0.3 0.55 1.92 3.4 4 4.5 5]
stepno_second	300	300	300
laser_shape	$'ideal'$	$'uniform'$	$'uniform'$
res_limit	0.3	0.3	0.3
fp_limit	0	$[0 : 0.01 : 0.15]$	0.1
innermost	15	15	15
gridsize	21	21	21

Variable	*Combined errors*	*Tetramer*
n_nmer	2	4
$fraction$	[0.5 0.5]	[0 0 0 1]
D	0.5	[0 0 0 0.5]
$D(2)$	$[1 : 0.1 : 2\ and\ 2.2 : 0.2 : 5]$	–
$aperture\_size\_x$	7	7
$aperture\_size\_y$	7	7
$density$	100	25
t_bleach	500	500
t_rec	1.5	2
$stepno\_second$	300	300
$laser\_shape$	$'diffraction'$	$'diffraction'$
res_limit	0.3	0.3
fp_limit	0.15	0.15
$innermost$	10	10
$gridsize$	21	21